BIOCHEMISTRY
including biophysical chemistry & molecular biology
Article

Biochemistry **2010,** *49,* 10045–10060 10045
DOI: 10.1021/bi101148w

Structural Origins of Nitroxide Side Chain Dynamics on Membrane Protein α-Helical Sites[†,‡]

Brett M. Kroncke,[§] Peter S. Horanyi,[∥] and Linda Columbus*[,§]

[§]*Department of Chemistry and* [∥]*Department of Molecular Physiology and Biological Physics, University of Virginia, Charlottesville, Virginia 22904, United States*

Received July 19, 2010; Revised Manuscript Received October 20, 2010

ABSTRACT: Understanding the structure and dynamics of membrane proteins in their native, hydrophobic environment is important to understanding how these proteins function. EPR spectroscopy in combination with site-directed spin labeling (SDSL) can measure dynamics and structure of membrane proteins in their native lipid environment; however, until now the dynamics measured have been qualitative due to limited knowledge of the nitroxide spin label's intramolecular motion in the hydrophobic environment. Although several studies have elucidated the structural origins of EPR line shapes of water-soluble proteins, EPR spectra of nitroxide spin-labeled proteins in detergents or lipids have characteristic differences from their water-soluble counterparts, suggesting significant differences in the underlying molecular motion of the spin label between the two environments. To elucidate these differences, membrane-exposed α-helical sites of the leucine transporter, LeuT, from *Aquifex aeolicus*, were investigated using X-ray crystallography, mutational analysis, nitroxide side chain derivatives, and spectral simulations in order to obtain a motional model of the nitroxide. For each crystal structure, the nitroxide ring of a disulfide-linked spin label side chain (R1) is resolved and makes contacts with hydrophobic residues on the protein surface. The spin label at site I204 on LeuT makes a nontraditional hydrogen bond with the *ortho*-hydrogen on its nearest neighbor F208, whereas the spin label at site F177 makes multiple van der Waals contacts with a hydrophobic pocket formed with an adjacent helix. These results coupled with the spectral effect of mutating the $i \pm 3, 4$ residues suggest that the spin label has a greater affinity for its local protein environment in the low dielectric than on a water-soluble protein surface. The simulations of the EPR spectra presented here suggest the spin label oscillates about the terminal bond nearest the ring while maintaining weak contact with the protein surface. Combined, the results provide a starting point for determining a motional model for R1 on membrane proteins, allowing quantification of nitroxide dynamics in the aliphatic environment of detergent and lipids. In addition, initial contributions to a rotamer library of R1 on membrane proteins are provided, which will assist in reliably modeling the R1 conformational space for pulsed dipolar EPR and NMR paramagnetic relaxation enhancement distance determination.

Site-directed spin labeling (SDSL)[1] is a powerful method uniquely suited for investigating structure and dynamics of soluble and membrane proteins of arbitrary molecular weight (*1*−*9*). In SDSL, a radical containing nitroxide spin label is site specifically introduced into a protein (e.g., selectively reacted with the free sulfhydryl of a single cysteine). The most commonly used spin label is a methanethiosulfonate derivative, designated R1, which is attached to the protein via a disulfide bond (Figure 1). The resulting electron paramagnetic resonance (EPR) spectrum of R1 reflects the overall rotational motions of the nitroxide ring on a nanosecond time scale (at X-band; 9.5 GHz). The dynamic modes that contribute to the motion of the nitroxide are (i) the intramolecular motion of the side chain, (ii) backbone motion (rigid body or oscillations about the backbone dihedral angles), and (iii) the overall rotational diffusion of the protein. For soluble proteins with a molecular mass ≥50 kDa and membrane-bound proteins, the contribution of the protein rotational diffusion to the EPR line shape is negligible (*1*, *6*). Several studies of α-helical soluble proteins have determined the backbone and side chain rotational contributions to the EPR line shape, allowing functionally relevant backbone dynamics to be investigated and quantified (*1*−*3*, *6*, *10*−*15*). However, quantifying dynamics with SDSL in membrane proteins has not yet been realized due to the complexity of the EPR spectra and the absence of high-resolution structures of spin-labeled α-helical membrane proteins. The aim of this study is to extend the soluble

[†]Use of the Advanced Photon Source was supported by the U.S. Department of Energy, Office of Science, Office of Basic Energy Sciences, under Contract No. W-31-109-Eng-38. Data were collected at the Southeast Regional Collaborative Access Team (SER-CAT) 22-ID (or 22-BM) beamline at the Advanced Photon Source, Argonne National Laboratory. Supporting institutions may be found at www.ser-cat.org/members.html. This work was supported by National Institutes of Health Grants RO1GM087828 (L.C.) and RO1GM079800 (P.S.H. and M.C.W.), National Science Foundation Grant MCB0845668 (L.C.), and Jeffress Memorial Trust (L.C.).

[‡]Protein Data Bank accession codes for crystal structures presented: 3MPN and 3MPQ.

*To whom correspondence should be addressed: phone, (434) 243-2123; fax, (434) 924-3710; e-mail, columbus@virginia.edu.

[1]Abbreviations: SDSL, site-directed spin labeling; EPR, electron paramagnetic resonance; SEHS, solvent-exposed α-helical sites; T4L, T4 lysozyme; MOMD, microscopic order macroscopic disorder; NMR, nuclear magnetic resonance; PRE, paramagnetic relaxation enhancement; PIPE, polymerase incomplete primer extension; OD, optical density; IPTG, isopropyl β-D-1-thiogalactopyranoside; TCEP, tris(2-carboxyethyl)phosphine; DDM, *n*-dodecyl β-D-maltopyranoside; MWCO, molecular weight cutoff; SDS−PAGE, sodium dodecyl sulfate−polyacrylamide gel electrophoresis; OG, *n*-octyl β-D-glucopyranoside; SER-CAT, Southeast Regional Collaborative Access Team; PEG-550 MME, polyethylene glycol 550 monomethyl ether; CCP4, Collaborative Computational Project 4; rmsd, root-mean-square deviation; PDB, Protein Data Bank; i.d., inner diameter; o.d., outer diameter; BSA, bovine serum albumin; CTACL, hexadecyltrimethylammonium chloride; DMSO, dimethyl sulfoxide.

Published on Web 10/21/2010

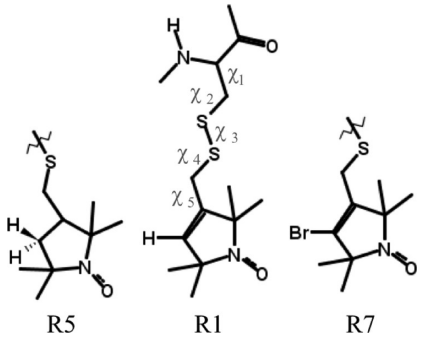

FIGURE 1: Nitroxide side chain structures. The most commonly used nitroxide side chain (R1) as well as two additional nitroxide side chains, R7 and R5, which have modifications of the nitroxide ring. The dihedral angles $\chi_1-\chi_5$ are labeled and are identical for the three side chains. R5 has a saturated bond in the nitroxide ring (the enantiomers can be separated and are designated R5(+) and R5(−)). R7 has a bromine atom attached to the 4-position of the ring.

protein efforts to α-helical membrane proteins, which have characteristically different EPR spectra (Figure 2), in order to expand the application of SDSL to include quantitative measurements of membrane protein dynamics.

Nitroxides at solvent-exposed α-helical sites (SEHS) on soluble proteins have little interaction with neighboring residues and, therefore, were investigated to quantify the internal nitroxide side chain dynamics (*2*, *14*, *15*). A motional model for R1 at SEHS on soluble proteins was elucidated using mutational analysis (*1*, *15*), systematic perturbation of the nitroxide probe (*2*, *10*, *15*), theoretical spectral fitting (*2*, *10*), and several crystal structures of T4 lysozyme (T4L) containing the R1 side chain (*11*−*14*). The R1 side chain was found to be ordered by an interaction between the S_δ of R1 with the C_α hydrogen of R1 (*12*−*14*, *16*), which reduces the amplitude of nitroxide motion as well as rates of motion about the first two bonds (defined by dihedrals χ_1 and χ_2; Figure 1). This restriction, together with the intrinsic barrier to rotation about the disulfide bond (χ_3) (*17*), leads to the "χ_4/χ_5" model (hereafter referred to as the *anisotropic-order* χ_4/χ_5 *model*) in which limited torsional oscillations about the two terminal bonds of the side chain largely determine the motion of the nitroxide ring (*10*). The motion of the nitroxide 2p molecular orbital is described using a microscopic order macroscopic disorder (MOMD) model (*18*) with simple anisotropic motion defined by an order parameter and an effective correlation time (*2*, *3*, *10*). Within the context of the anisotropic-order χ_4/χ_5 model, the quantified internal modes of R1 are independent of position along the solvent face of an α-helix, and variations in line shape among structurally similar sites should reflect contributions from other dynamic modes, namely, backbone fluctuations. The potential of quantifying backbone dynamics using this R1 motional model was demonstrated by comparing the dynamics measured with SDSL to those determined with NMR for the DNA-binding domain of GCN4 (*2*).

EPR spectra of aqueous solvated residues at SEHS have characteristic differences from analogous sites exposed to an aliphatic environment (Figure 2). The aliphatic solvated residues have spectra that are broader and frequently contain multiple components (labeled α and *β* in Figure 2). To understand the differences between EPR spectra of α-helical soluble and membrane proteins, we chose to investigate SEHS sites on the leucine transporter, LeuT, of *Aquifex aeolicus*, which were analogous to the solvent-accessible sites already studied on T4L (*19*). Specifically,

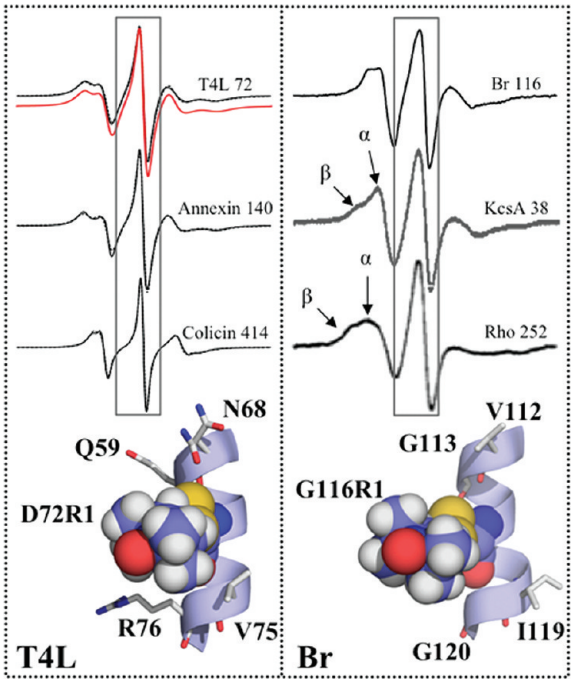

FIGURE 2: Solvent-exposed helical sites (SEHS) of soluble and membrane proteins. Representative EPR line shapes of R1 at SEHS of soluble (T4L (*10*) and the soluble forms of annexin (*57*) and colicin (*58*); spectral fit of T4L 72R1 in solid red below the experimental spectrum) and membrane proteins (bacteriorhodopsin (Br) (*59*), the potassium channel KcsA (*33*), and rhodopsin (Rho) (*34*)) are shown for comparison. The boxes highlight the central line of SEHS on soluble and membrane proteins, which are typically broader for membrane proteins, one of the spectral differences between the SEHS. Multiple spectral components are labeled α (mobile) and *β* (immobile). Molecular models are shown to compare the environment of T4L and bacteriorhodopsin SEHS. The $i \pm 3, 4$ are rendered in stick, and the nitroxide is represented in a sphere filling model.

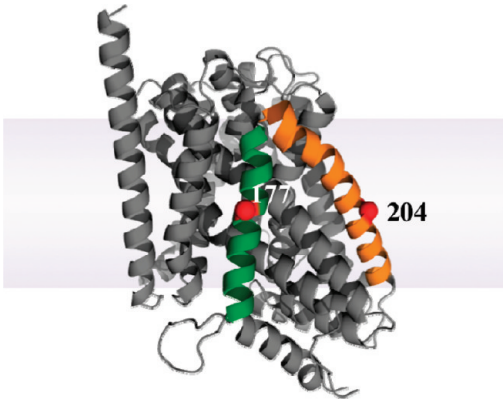

FIGURE 3: Spin-labeled sites on LeuT. Crystal structure of LeuT (PDB ID 2A65 (*19*)) with F177 and I204 α-carbons displayed as red spheres. Site F177 is located in the center of helix 4 (green), and I204 is in the middle of helix 5 (orange).

residues F177 and I204 were chosen as possible SEHS because modeling of R1 indicated these sites potentially lacked tertiary contacts, were solvent exposed, and were not located at lattice contact sites (Figure 3).

The structures for R1 residues at two SEHS sites are presented, and in both cases, electron density of the nitroxide ring is observed due to interactions with the protein environment. In each case, the R1 side chain adopts the {**m**,**m**} rotamer (dihedral convention of Lovell et al. (*21*) is used; $\{\chi_1, \chi_2\}$; $\mathbf{m} = -60° \pm 20°$,

p = +60° ± 20°, and **t** = 180° ± 20°), and the $C_\alpha-H\cdots S_\delta$ interaction is observed. Although these conformers suggest a χ_4/χ_5 model similar to that used for SEHS sites in T4L, the additional interactions between R1 and the protein surface appear to alter the motional model (hereafter referred to as *anisotropic-rate* χ_4/χ_5 *model*). In addition, mutagenesis, theoretical spectral fits, and temperature studies suggest that many weak interactions stabilize the nitroxide ring on the hydrophobic surface of the protein resulting in a highly anisotropic motion (both in rate and order) of the nitroxide. The results of this study provide a starting point for determining a motional model for R1 on membrane proteins allowing quantification of nitroxide dynamics in the aliphatic environment of detergent and lipids. In addition, initial contributions to a rotamer library of R1 on membrane proteins are provided, which will assist in reliably modeling the R1 side chain for pulsed dipolar EPR distance determination (*22*) as well as NMR-based paramagnetic relaxation enhancement (PRE) distance measurements (*23*).

MATERIALS AND METHODS

Cloning, Expression, and Purification of LeuT Mutants. The plasmid pET16b containing the LeuT gene was a generous gift from Dr. Eric Gouaux (Vollum Institute, Oregon). All cysteine and alanine mutations were introduced using PIPE mutagenesis (*24*). Mutants were confirmed by sequencing the entire gene (Genewiz Inc., South Plainfield, NJ). Expression and purification of LeuT were performed according to a previously described protocol (*19*). The DNA for the LeuT pET16b construct encoding a C-terminal eight His tag was transformed into C41 (DE3) cells. Cells were grown at 310 K to an OD_{600} of 0.6−0.8 in Terrific broth and induced with 100 μM IPTG for 20 h at 293 K. The cells were resuspended and lysed in 20 mM Tris-HCl (pH 8.0), 190 mM NaCl, 10 mM KCl, and 1 mM lysis buffer. After the cells were lysed, the cell debris was removed by centrifugation at 15000*g* for 60 min. The cell membranes were isolated from the supernatant by centrifuging at 142200*g* for 210 min. The resulting pellet was resuspended in 50 mL (for 3 L of cell culture) of lysis buffer with 40 mM DDM (Anatrace, Inc., Maumee, OH) and stirred overnight at 277 K. Afterward, the suspension was passed through a Co^{2+}-affinity column equilibrated with 10 column volumes of lysis buffer. The column was washed with 15 column volumes of lysis buffer with 1 mM DDM and 20 mM imidazole and eluted in 10 column volumes of lysis buffer with 1 mM DDM and 300 mM imidazole.

Spin Labeling of LeuT Mutants. The eluted fraction was concentrated and passed through a PD-10 column (GE Healthcare Bio-Sciences Corp., Piscataway, NJ) to remove TCEP and imidazole and to exchange the buffer (pH was adjusted from 8.0 to 7.0 for higher labeling efficiency). The PD-10 column eluate was incubated with a 5-fold molar excess of (1-oxy-2,2,5,5-tetramethyl-3-pyrroline-3-methyl)methanethiosulfonate, R1 (a gift from Wayne Hubbell, UCLA, and Kálmán Hideg, University of Pécs), or 4-bromo-(1-oxy-2,2,5,5-tetramethyl-3-pyrroline-3-methyl)-methanethiosulfonate, R7, or (±)-(1-oxy-2,2,5,5-tetramethylpyrrolidin-3-yl)methyl methanethiosulfonate, R5(±), (Toronto Research Chemicals Inc., Toronto, Canada) at room temperature overnight to ensure complete labeling. To remove the His tag, the spin-labeled protein was incubated with 75 μg of thrombin (MP Biomedicals, Solon, OH) for 3 h at room temperature. The digested solution was passed through 0.5 mL of a *p*-aminobenzamidine−agarose (Sigma-Aldrich, St. Louis, MO) resin to remove the thrombin. The flow-through was concentrated and purified further using a HiPrep Sephacryl S200HR 320 mL column (GE Healthcare Bio-Sciences Corp., Piscataway, NJ) equilibrated with 20 mM Tris-HCl (pH 7.0), 190 mM NaCl, 10 mM KCl, and 40 mM OG. The eluted fraction was dialyzed in a 3.5 kDa MWCO dialysis cassette (Thermo Scientific, Rockford, IL) against 0.25 L to a concentration of 10 mM Tris-HCl (pH 7.0), 45 mM NaCl, 5 mM KCl, and 40 mM OG overnight at 277 K. SDS−PAGE was used to analyze fractions and assess cleavage and protein purity.

The spin-labeling procedure outlined above results in a background signal as is evident in the spectrum obtained with the cysteine-less LeuT construct (Figure S1, panel A). For cysteine mutants of LeuT, the background signal is approximately 5% the intensity of the EPR spectrum (Figure S1). To reduce the background signal of spin-labeled samples, the solutions were incubated at room temperature for approximately 3 days before being passed through a PD-10 column (loaded <200 μL and eluted into 3.5 mL) to remove the unreacted spin label, reducing the background signal to less than 1% (Figure S1, panel B).

X-ray Crystallography of Spin-Labeled LeuT Mutants. Crystals were grown using sitting drop vapor diffusion with a well solution of 0.1 M HEPES−NaOH (pH 7.0), 22−28% PEG-550 MME, and 0.2 M NaCl. Crystallization drops consisted of 1 μL of ~7 mg/mL LeuT and 1 μL of well solution. The crystals were grown at 293 K and took approximately 10−15 days to form dimensions of $\sim 50 \times 100 \times 100$ μm. The crystals were harvested in a cryoprotectant of 35% PEG-550 MME and 40 mM OG. The looped crystals were then plunged into liquid nitrogen under a stream of gas to reduce the freezing time and improve diffraction (*25*). Data were collected at an X-ray wavelength of 1.0 Å at the SER-CAT 22-ID beamline at the Advanced Photon Source, Argonne National Laboratory.

The data were processed using HKL2000 (*26*), and the structures were solved and subsequently refined using REFMAC (version 5.5.0088) from the CCP4 suite (*27*). Model building and real space refinement were done using COOT (*28*). Each of the final structures was validated using Molprobity (*29*), and the structures were deposited under the following accession numbers: 3MPN (F177R1) and 3MPQ (I204R1). Although weak at 1.0 Å, anomalous scattering of the sulfur was investigated to further position the disulfide of the nitroxide side chain, and anomalous maps were obtained for each structure; however, the anomalous signal was indeed below the noise at 1.0 Å. The data collection and processing statistics are given in Table 1. All protein figures were rendered with Pymol (*30*).

EPR Spectroscopy of Spin-Labeled LeuT Mutants. The room temperature X-band EPR spectroscopy was performed on a Bruker EMX spectrometer with an ER4123D dielectric resonator (Bruker Biospin, Billerica, MA). All samples were in the crystallization buffer of 10 mM Tris-HCl (pH 7.0), 45 mM NaCl, 5 mM KCl, and 40 mM OG unless explicitly stated otherwise. X-band temperature series were performed on an ELEXSYS E-500 spectrometer from Bruker with a high sensitivity cavity resonator or on an E-line 102 Century series spectrometer from Varian with a loop gap resonator. Protein samples of 5 μL (≈100 μM) were loaded into Pyrex capillaries (0.60 mm i.d. ×0.84 mm o.d.; Fiber Optic Center, Inc., New Bedford, MA). Q-band EPR spectroscopy was performed on an ELEXSYS E-500 spectrometer from Bruker with an ER5106 QT-W resonator with protein samples of 5 μL (≈100 μM) in quartz capillaries (0.60 mm i.d. ×0.84 mm o.d.;

Table 1: Data Collection and Refinement Statistics

	LeuT F177R1	LeuT I204R1
data collection		
wavelength (Å)	1.0	1.0
resolution range (Å)[a]	36.80−2.25 (2.31−2.25)	43.67−2.25 (2.31−2.25)
total reflections[b]	113409 (112864)	117833 (117522)
unique reflections	28364	27874
R_{sym} (%)[a]	13.0 (35.9)	19.3 (28.5)
I/σ[a]	13.0 (3.1)	18.6 (4.7)
completeness (%)[a]	98.6 (89.1)	97.6 (85.6)
redundancy	4.1 (3.1)	4.2 (4.0)
space group	*C*2	*C*2
unit cell dimensions		
β (deg)	95.35	95.26
a (Å)	87.261	87.702
b (Å)	86.222	86.712
c (Å)	80.636	80.866
refinement		
resolution (Å)	36.80−2.25	43.67−2.25
reflections used	26547	26460
R_{cryst} (%)[c]	17.4	18.5
R_{free} (%)[d]	21.4	22.3
average B value (Å)	26.2	36.5
rms deviations		
rmsd bond lengths (Å)	0.02	0.02
rmsd bond angles (deg)	1.77	1.72
PDB accession code	3MPN	3MPQ

[a]Numbers in parentheses are for the outer shell. [b]Numbers in parentheses are the used reflections. [c]$R_{cryst} = \sum_{hkl}||F_o| - |F_c||/\sum_{hkl}|F_o|$, where F_o and F_c are the observed and calculated structure factors, respectively. [d]R_{free} is R_{cryst} calculated using 5% of the data, randomly chosen and omitted for refinement.

Fiber Optic Center, Inc., New Bedford, MA). The solutions for 200 K Q-band spectra had 10% (v/v) glycerol as a glassing agent.

Fitting of EPR Spectra. Frozen spectra (200 K) at Q- and X-band were fit using an effective Hamiltonian rigid limit model implemented in a Labview program written and provided by Christian Altenbach and Wayne L. Hubbell, University of California, Los Angeles. EPR spectra recorded between 273 and 313 K were fit using the MOMD model implemented in the NLSL program of Freed and co-workers (*18*). The magnetic parameters used in the MOMD fits were determined from the effective Hamiltonian fits of the Q- and X-band frozen spectra. In the MOMD model, three-coordinate frames are employed to represent the internal motion of the nitroxide in the protein, as illustrated in Figure 4. The molecule-fixed magnetic tensor frame (x_M, y_M, z_M) has z_M along the nitroxide 2p molecular orbital, x_M lies along the NO bond axis, and y_M is selected for a right-handed coordinate system. The magnetic frame is the principal frame for both the nitroxide hyperfine **A**- and **g**-tensors. The second coordinate frame is the principal frame of the rotational diffusion tensor (x_R, y_R, z_R). In general, the rotational diffusion and magnetic frames are not coincident and are related by a set of three Euler angles (γ_D, β_D, α_D) (Figures 4 and S2). Anisotropic motional restrictions are simulated in the MOMD model by introducing a restoring (ordering) potential (U) that constrains the motion of z_R. Most fits of EPR spectra of spin-labeled proteins use the simple restoring potential $U(\theta) = -(1/2)k_BTc_0^2(3\cos^2\theta - 1)$, where c_0^2 is a scaling coefficient and θ is the (instantaneous) angle between z_R and the symmetry axis of the potential. The symmetry axis of the potential defines the *z*-axis of the third and final coordinate frame, the director frame. The director frame is uniaxial (z_D) and fixed with respect to the protein. The existence of the restoring potential results in an anisotropic motion and can be characterized by the order parameter $S = -(1/2)\langle(3\cos^2\theta - 1)\rangle$, where the brackets indicate spatial averaging. For an individual protein molecule, z_D forms an angle ψ with respect to the external magnetic field. To obtain the final spectrum corresponding to an isotropic distribution of protein orientations, the spectra are summed over ψ. To fit the experimental spectra, only the rotational rates, a single coefficient for the restoring potential, and the Euler angles were allowed to vary one at a time. After a satisfactory fit was obtained, the Lorentzian and Gaussian line widths were allowed to vary while constrained to 1 G or less. Once the best fit was obtained, the **g**- and **A**-tensors were allowed to vary by 0.0005 and 0.75 G, respectively. The goodness of fit was assessed using the reduced χ^2 (*18*) between the theoretical and experimental spectra (Tables S1 and S2) as well as a visual assessment of the salient features of the experimental spectrum (specifically the high-field manifold).

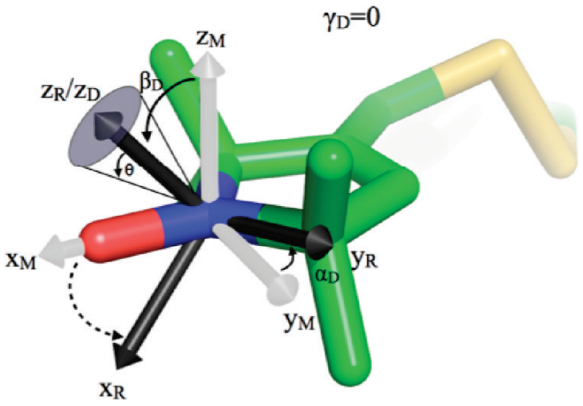

FIGURE 4: Dynamic model for fitting EPR spectra. A diagram showing the relationship between the nitroxide magnetic frame (z_M, y_M, and x_M; gray), the diffusion frame (x_R, y_R, z_R; black), and the protein fixed director (z_D) taken to lie along the *z*-axis of the diffusion frame at equilibrium. The Euler angles are defined by an order of rotations: (1) a rotation about z_M of γ_D, (2) a rotation about y_D of β_D, and (3) a rotation about z_D of α_D. With these definitions of γ_D, β_D, and α_D, the angle β_D defines the fixed tilt of z_R with respect to z_M. The ordering potential is defined as a function of angle θ (the instantaneous angle between z_R and z_D) that defines the barrier of rotation for y_R and x_R. The arrows show the mapping of the magnetic frame to the diffusion frame (the solid arrows correspond directly to a particular Euler angle).

RESULTS

To investigate the molecular origins of the nitroxide motions that give rise to EPR line shapes observed on the surfaces of α-helical membrane proteins, we chose LeuT as a model protein because high-resolution (1.65 Å) X-ray crystal structures were attainable (*19*) and the native sequence lacks cysteine residues. High-resolution diffraction data were required to identify major side chain conformations potentially important in analyzing R1 EPR spectra. The resolution of 2.25 Å for both structures (F177R1 and I204R1) determined is likely sufficient for observing multiple side chain rotamers (*31*). Sites F177 and I204 (Figure 3) were selected for structure determination because modeling of R1 suggested these sites could be SEHS comparable to T4L D72, a site used to

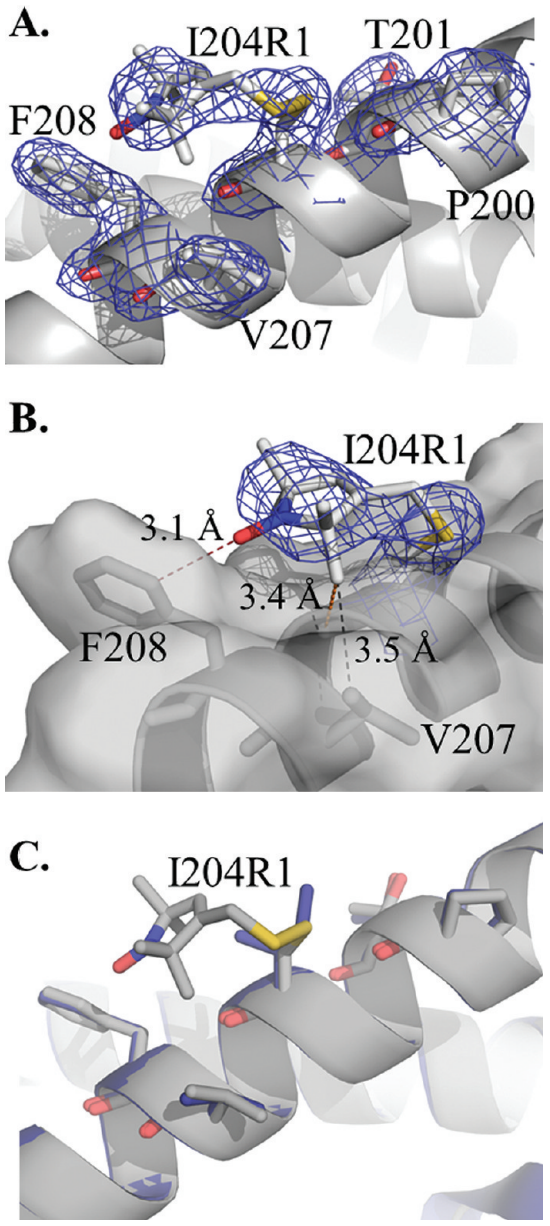

FIGURE 5: X-ray crystal structure of I204R1. (A) Electron density shown as a blue mesh superimposed on the stick model of R1 and neighboring side chains. The $2F_o - F_c$ map is contoured at 1.3σ. (B) Interactions of I204R1 with $i + 3$, 4 residues. The R1 side chain is shown in stick with the electron density shown as a blue mesh superimposed, and the helix is rendered with a transparent surface with F208 and V207 shown as sticks. The R1 nitroxide ring interacts with F208, V207, and its own carbonyl. (C) Superposition of the I204R1 structure on the wild-type structure. The wild-type LeuT (blue) and the I204R1 (colored by atom) structures were pairwise compared using DaliLite (*60*) with the best structural alignment shown.

investigate the anisotropic-order χ_4/χ_5 motional model of R1 on SEHS of soluble proteins (*10*).

Structure of I204R1. The structure of I204R1 was determined at 100 K and refined to 2.25 Å resolution with an R_{cryst} and R_{free} of 18.5% and 22.3%, respectively (Table 1). A single conformation of the R1 side chain was observed, and the entire side chain was resolved (Figure 5A,B) allowing $\chi_1-\chi_5$ to be determined (Table 2). The side chain adopts an {**m**,**m**} rotameric state similar to that observed for {**m**,**m**} conformations of R1 on T4L (*11*−*14*). The observed R1 conformer retains the $C_\alpha-H\cdots S_\delta$ interaction (Table 2) reported in soluble proteins (*11*−*14*). The I204R1 and wild-type structures are nearly identical (all atom pairwise root-mean-square deviation (rmsd) of 0.20 Å); however, χ_2 for the wild-type residue I204 is 170° {**m**,**t**} whereas I204R1 is −60° (Figure 5, C). Although the {**m**,**t**} conformer of R1 is sterically allowed, the $C_\alpha-H\cdots S_\delta$ interaction cannot be formed in this configuration, suggesting this interaction may influence the rotamer population (*11*).

Structures of R1 at SEHS on T4L have all lacked interactions between the nitroxide ring and the protein environment, and electron density was not observed beyond the distal sulfur of the side chain (*11*−*14*). In the case of I204R1, density was observed for the entire side chain due to interactions with residues within the same helix. I204R1 interacts with its own carbonyl backbone oxygen as well as residues F208 and V207 (Figure 5B). The nitroxide oxygen is 3.1 Å from the *ortho*-carbon ($C_{\delta1}$) of F208, and with hydrogen atoms modeled, the O···H distance is 2.2 Å with a N−O···H angle of 160° and C−H···O angle of 140°, suggesting a hydrogen bond interaction (*32*). A nearly identical interaction was previously observed at site 75 on T4L; however, the hydrogen bond was made to a phenylalanine on a symmetry-related molecule and was presumably not present in solution (*14*). The strengths of similar nontraditional hydrogen bonds were measured to be around 1−3 kcal mol^{-1} (*17*) and would likely restrict the motion of the spin label. In addition to the hydrogen bond, one of the nitroxide ring methyl groups resides in close contact with a methyl from V207 and its own carbonyl oxygen. With hydrogen atoms modeled, the C−H···H−C distance (2.2 Å) and the C−H···O distance (2.4 Å) are less than the sum of the van der Waals radii, suggesting an attractive interaction; however, the lack of spectral change when V207 is mutated to an alanine residue suggests the interaction is weak (see below).

Temperature Dependence of I204R1. The line shape of I204R1 (Figure 6) is consistent with spectra observed for detergent-exposed helical sites (*33*−*36*) such as I38R1 on KcsA (Figure 2). I204R1 has broad spectral features compared to analogous sites on soluble proteins and has two spectral components (labeled α and β in Figure 6). To investigate which population (α or β) was likely represented in the crystal structure, the temperature dependence of the EPR line shape was investigated between 274 and 314 K (Figure 6). The spectral populations are modulated by temperature with the immobile β-population more predominant at lower temperatures. At temperatures 304 K and above, the β-component is barely visible. Although the α-population becomes more immobile at lower temperatures (as expected), the populations are easily distinguishable above ~280 K. The temperature-induced changes in spectral population suggest the β-population of I204R1 is most similar to the spin label rotamer observed in the 100 K crystal structure.

Interactions of I204R1 in Solution. In order to determine a correlation between the observed crystal structure and solution EPR spectrum, mutagenesis was employed. Figure 7 shows the EPR spectra of I204R1 with wild-type $i \pm 3$, 4 neighbors compared to the single alanine mutation at these positions. The spectrum for the P200A/I204R1 mutant is not shown because the protein did not overexpress. The only mutation that resulted in a significant change in the EPR line shape is F208A/I204R1, which is in agreement with the structure in which F208 makes the closest contacts with R1 (Figures 5 and S3). The F208A mutation reduces the β-population by 10−20% (determined from spectral fits) corresponding to a change in ΔG of ~1 kcal; however, the mutation also decreases the mobility of the α-population.

Table 2: R1 Dihedral Angles at α-Helical Sites in LeuT

LeuT mutant	rotamer	χ_1 (deg)	χ_2 (deg)	χ_3 (deg)	χ_4 (deg)	χ_5 (deg)	$C_\alpha\cdots S_\delta$ (Å)	$C_\alpha{-}H\cdots S_\delta$ (Å)	$<C_\alpha{-}H\cdots S_\delta$ (deg)
F177R1	{**m**,**m**}	−69	−57	107	103	−24	3.3	2.5	124.4
I204R1	{**m**,**m**}	−69	−59	−87	71	−95	3.5	2.9	115.0

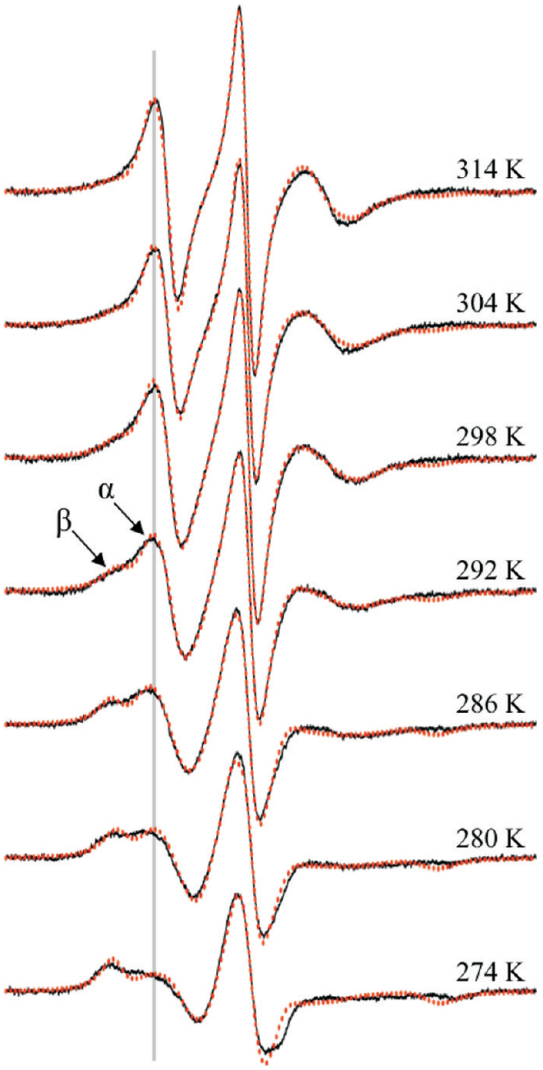

FIGURE 6: Temperature dependence of I204R1. The experimental spectra (black) and the theoretical fits (dotted red) are superimposed on the experimental spectra. The two populations are labeled α (mobile component) and β (immobile component). A gray line is drawn to guide the eye.

The effect of the F208A mutation on the I204R1 spectrum is more dramatic at 280 K (Figure S3). One explanation for the observed populations and mobility of I204R1 is that the nitroxide ring forms additional interactions (weaker than the nontraditional hydrogen bond) with the resulting surface upon removal of the phenyl group. Another possibility is that the F208A mutation disrupts the tertiary interaction between helix 5 and the neighboring helix 8 (F208 directly interacts with residues L340 and L343). The resulting structural rearrangement may modulate the motion of helix 5 or create additional interactions of R1 with the protein due to slight helix rotation; however, without a crystal structure, the consequence of the mutation is only speculative.

Structure of F177R1. The structure of F177R1 was determined at 100 K and refined to 2.25 Å resolution, with an R_{cryst} and R_{free} of 17.4% and 21.4%, respectively (Table 1). A single conformation of the R1 side chain was observed, and the entire side chain was resolved (Figure 8) allowing $\chi_1{-}\chi_5$ to be determined (Table 2). The side chain adopts an {**m**,**m**} rotameric state similar to that observed for I204R1 and for {**m**,**m**} conformations of spin-labeled sites on T4L. The nitroxide side chain χ_2 differs from the wild-type phenylalanine residue by 112°, positioning the nitroxide ring toward helix 9 rather than the N-terminus of helix 4 (Figure 8C). The F177R1 and wild-type structures are nearly identical (all atom pairwise root-mean-square deviation (rmsd) of 0.20 Å); however, L173 is displaced (χ_2 of 168° in the wild-type structure and −135° in the R1 structure) and interacts with the nitroxide ring.

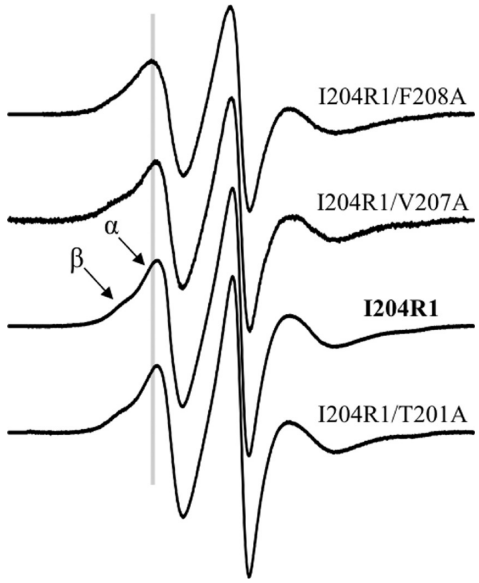

FIGURE 7: X-band EPR spectra of I204R1 with the $i \pm 3, 4$ alanine mutations. The two spectral components are labeled α (mobile component) and β (immobile component). A gray line is drawn to guide the eye.

The nitroxide ring of F177R1 fits into a hydrophobic pocket on the surface of helices 4 and 9 (Figure 8B). The pocket is formed by L173, M176, L380, A383, A384, and F387. Three of the four methyl groups on the nitroxide ring (C6, C8, and C9) contact surrounding residues. Multiple contacts of the nitroxide ring methyl groups with surrounding hydrophobic residues have been observed previously with tertiary contact or buried sites on T4L, such as K65R1 (*14*), L118R1, and T115R1 (*13*), but not on SEHS. The closest contacts with F177R1 are between a distal methyl of L173 and methyl C6 (C···C distance of 3.8 Å), the C_β of M176 and methyl C8 (C···C distance of 4.2 Å), a distal methyl of L380 and methyl C9 (C···C distance of 4.1 Å), the C_β of A383 with the methyl groups C8 and C9 (C···C distance of 3.9 Å), and C_β of F387 and methyl C8 (C···C distance of 4.0 Å), and the C_β of V180 interacts with the C_ε of R1 (C···C distance of 4.3 Å). In addition, the oxygen of the nitroxide moiety interacts with the C_α and C_β of A384 (C···O distance of 3.9 Å). Although significant interactions between R1 and the protein surface are

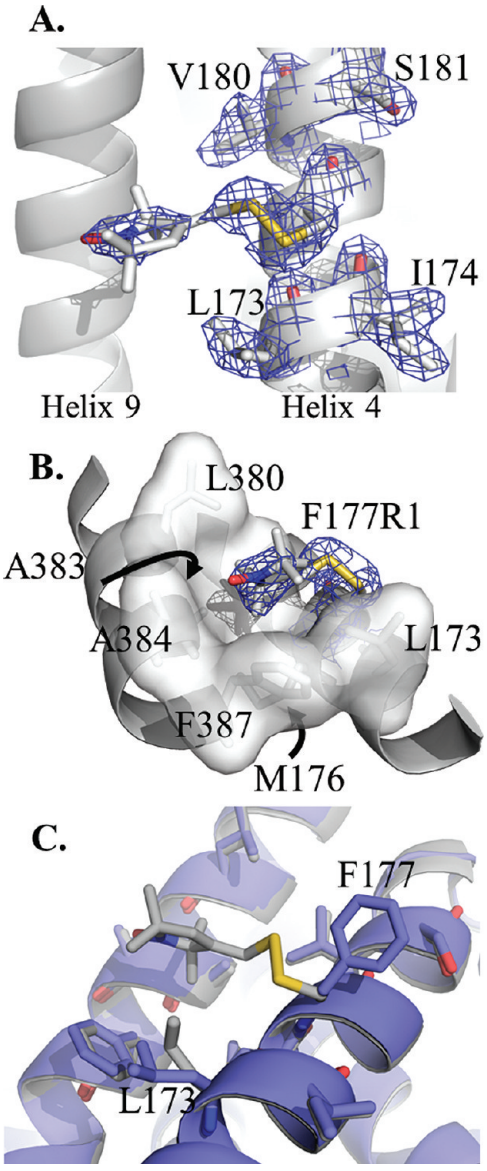

FIGURE 8: X-ray crystal structure of F177R1. (A) Electron density superimposed on the stick model of R1 and neighboring side chains. The $2F_o - F_c$ map is contoured at 1.3σ. (B) Interactions of F177R1 with surrounding residues. The R1 side chain is shown in stick model with the electron density, shown as a blue mesh, superimposed on top. Helices 4 and 9 are rendered with a translucent van der Waals surface with residues forming the contact surface shown as gray sticks. (C) Superposition of the F177R1 structure on the wild-type structure. The wild-type LeuT (blue) and the F177R1 (colored by atom) structures were pairwise compared using DaliLite (*60*) with the best structural alignment shown.

observed, the ring density is weaker than in I204R1, indicating a larger degree of dynamic or static disorder.

Temperature Dependence of F177R1. The line shape of F177R1 (Figure 9) is consistent with spectra observed for detergent-exposed helical sites (*33*−*36*). F177R1 is a single component spectrum with significant broadening compared to soluble protein counterparts (Figure 2). To determine if the conformer in solution at room temperature is consistent with the 100 K crystal structure, the F177R1 EPR spectrum was investigated as a function of temperature (between 278 and 308 K), and spectra are shown in Figure 9. With decreasing temperature, the spectra are broadened due to the decrease in spin label mobility. Unlike I204R1, an additional spectral component is not observed

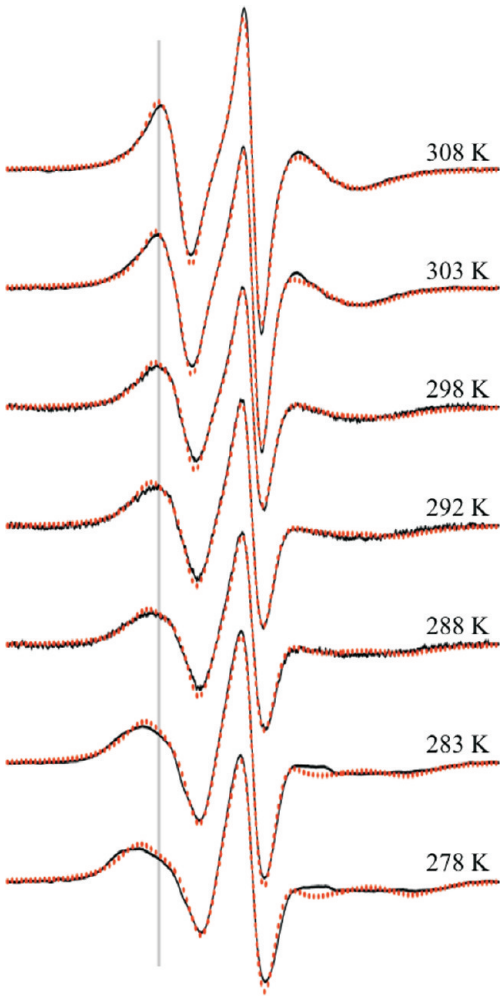

FIGURE 9: Temperature dependence of F177R1. The experimental spectra (black) with the theoretical fits (dotted red) superimposed. A gray line is drawn to guide the eye.

at room temperature or at lower temperatures. Therefore, the crystal structure of F177R1 likely represents the rotameric state observed at room temperature.

Interactions of F177R1 in Solution. In order to further investigate a correlation between the solution EPR spectrum of F177R1 and the conformer observed in the crystal structure, mutagenesis was employed. Figure 10 shows the EPR spectra of F177R1 with wild-type $i \pm 3$, 4 neighbors compared to the single alanine mutation at these positions. Mutations S181A and V180A do not affect the EPR spectrum of F177R1 consistent with the crystal structure in which interactions are not observed between the R1 side chain and the $i + 3$, 4 residues. The L173A mutation modulates the EPR line shape as expected from the interaction observed in the crystal structure. With the L173A mutation, the EPR spectrum of F177R1 has two spectral components, one similar to F177R1 and one more immobile (arrow, Figure 10). An explanation of the spectral effect of this mutation in terms of simple interactions between the spin label and L173 is not possible because both L173 and F177R1 interact with helix 9 (Figure 8). Therefore, the introduced cavity could modulate the interaction with R1 but could also disrupt the tertiary contact and packing between helices 4 and 9. A crystal structure of this mutant may aid in the interpretation of the EPR line shape changes.

Unexpectedly, the I174A mutation also affects the EPR line shape of F177R1. In the crystal structure, I174 does not make

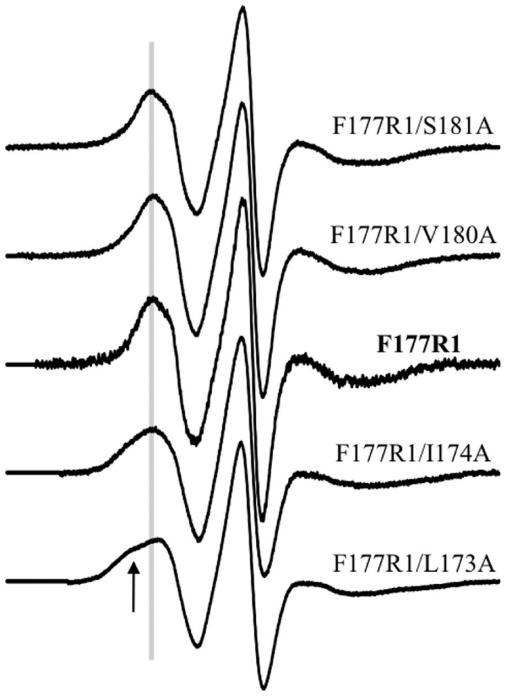

FIGURE 10: X-band EPR spectra of F177R1 and $i \pm 3$, 4 alanine mutations. An arrow indicates a second spectral component, and a gray line is drawn to guide the eye. The spectra were shifted to ensure the central line crossing zero on the *y*-axis was in the center of the spectrum; zeros were then added to ensure uniform spectral width.

direct contacts with F177R1. However, as proposed for F208A/I204R1, the resulting cavity due to the mutation may stabilize an alternative R1 conformation. It is worth noting that three of the six ordered detergent molecules observed in the crystal structures of LeuT pack about helices 4 and 9 with one in direct contact with I174 (Figure S4). Therefore, an alternative explanation is that the alanine mutation may disrupt the detergent packing around the helix, which could modulate the conformation and/or dynamics of helix 4.

Magnetic Parameters of Nitroxides on Detergent-Exposed Helical Sites. To quantitatively understand the dynamics of the nitroxide probe, the EPR spectra need to be theoretically fit with a motional model. To reduce the number of varied parameters in the spectral fitting using the MOMD model (*18*) (from 14 to 8 parameters for a single spectral component), the magnetic parameters for R1 at F177R1 and I204R1 were determined in the detergent environment by recording Q- and X-band spectra of F177R1 and R7 and I204R1 and R7 at 200 K (Q-band shown in Figure S5). At 200 K, the correlation time of the spin label is reduced, and the resulting spectra should reflect the rigid limit for which magnetic parameters can be directly measured. To ensure that internal motions were sufficiently reduced, the R7 derivative was also investigated. The addition of a 4-substituent on the ring of the R1 spin label was previously shown to greatly reduce the motion about the χ_5 dihedral angle (*1*, *37*). The spectra of R1 and R7 at each site are nearly identical, indicating that the internal side chain dynamics are not contributing to the spectrum and indeed this spectrum is representative of the rigid limit. Each spectrum was fit with an effective Hamiltonian rigid limit model. The values of the **A**- and **g**-tensor elements from the fits were $g_{xx} = 2.0084$, $g_{yy} = 2.0058$, $g_{zz} = 2.0020$, $A_{xx} = 5.1$, $A_{yy} = 5.3$, and $A_{zz} = 34.3$. These values are similar to previously published values for nitroxide spin labels in organic solvents (*38*).

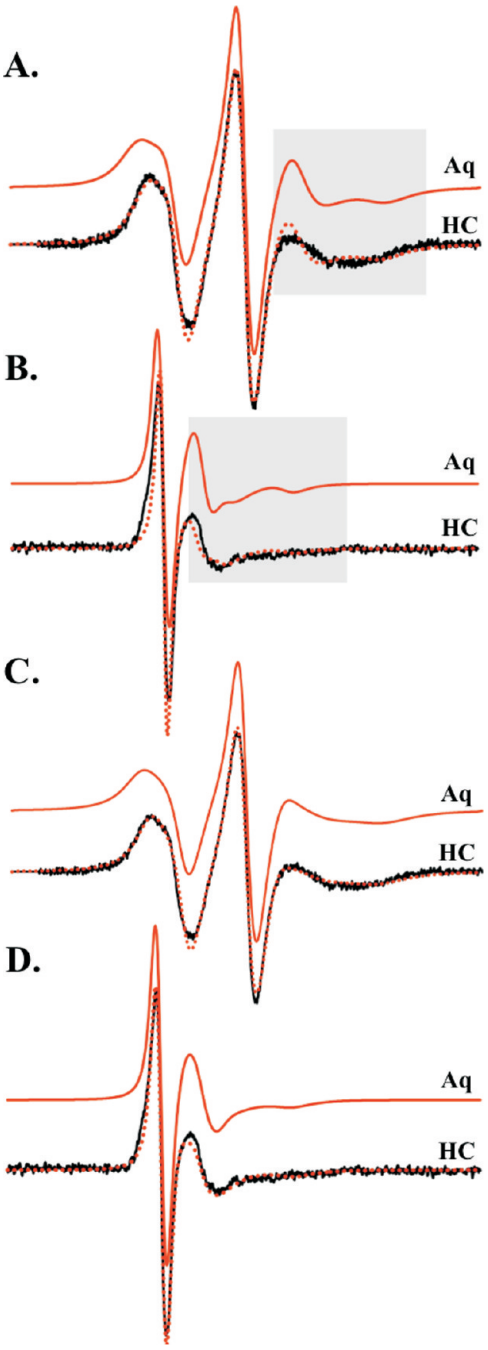

FIGURE 11: (A, B) Best spectral fit of F177R1 using anisotropic-order χ_4/χ_5 motional model of R1 at SEHS. The X-band (A) and Q-band (B) experimental spectra (black) and the theoretical fits (dotted red) for site F177R1 are shown. The theoretical fit using aqueous magnetic parameters (top, solid red spectrum, labeled Aq) and the fit using the experimentally determined hydrophobic magnetic parameters (dotted red spectrum, superimposed, labeled HC) are shown for each fit. The dynamic parameters of the anisotropic-order χ_4/χ_5 model for SEHS of soluble proteins (Table 3) (*10*) were used for the fits. The gray boxes highlight the high-field line shape features that are not fit well with the anisotropic-order χ_4/χ_5 model. (C, D) Best spectral fit of F177R1 at X-band (C, 100 G) and Q-band (D, 200 G) experimental spectra (black) and the theoretical fits (dotted red, superimposed) for site F177R1 are shown. The theoretical fit using aqueous magnetic parameters (top, solid red spectrum, labeled Aq) and the fit using the experimentally determined hydrophobic magnetic parameters (dotted red, superimposed, labeled HC) are shown for both X- and Q-band spectra. The dynamic parameters for the fits are given in Table 3.

Motional Models of R1 on Detergent-Exposed Helical Sites. To determine if the line shape differences between soluble

Table 3: Dynamic Parameters for Theoretical Fits[a]

LeuT mutant	R_x[b] (τ, ns)	R_y[b] (τ, ns)	R_z[b] (τ, ns)	S	$\langle\theta\rangle$ (deg)	β (deg)	α (deg)[e]
F177R1[c]	7.75 (3.0)	7.95 (1.9)	7.73 (3.1)	0.36	41	41	−2
F177R1	7.50 (5.3)	7.98 (1.8)	< 7.00 (> 16)[d]	0.24	45	0	−57
F177R5(+)	7.45 (5.9)	8.07 (1.4)	7.05 (15)	0.24	45	0	−58
I204R1(α)	7.58 (4.4)	8.14 (1.2)	< 7.00 (> 16)[d]	0.15	49	0	−43
I204R1(β)	7.20 (11)	7.58 (4.4)	6.80 (26)	0.38	40	0	−90
I204R5(+)	7.45 (5.9)	8.09 (1.4)	7.23 (9.8)	0.18	46	6	−45

[a]The range for each value is given in Table S1. [b]Values reported as $\log(R_i/s^{-1})$, where $i = x$, y, or z. [c]Anisotropic-order χ_4/χ_5 model. [d]The spectra are insensitive to R_z values < 7.0 (Figure S10). [e]The spectral calculation is insensitive to the sign of α. For the purpose of interpretation using the anisotropic-rate χ_4/χ_5 model (Figure S2C), the sign is taken to be negative.

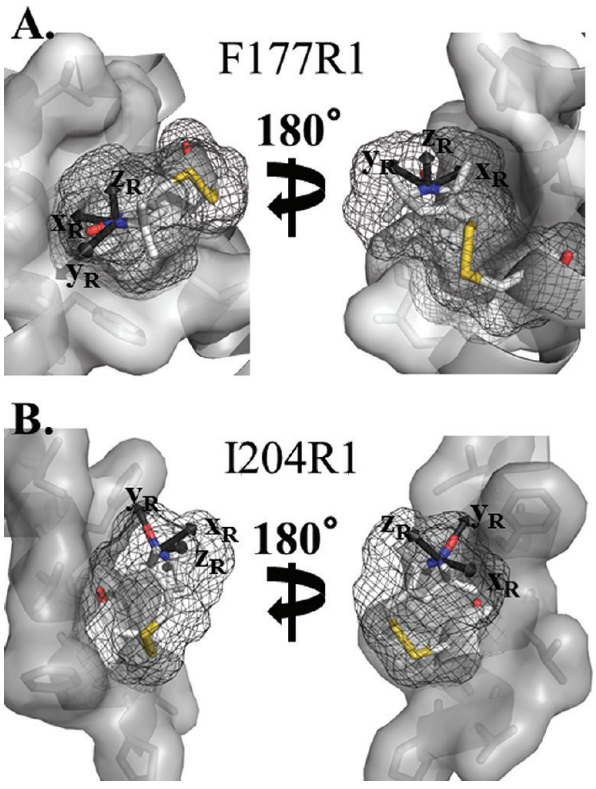

FIGURE 12: Comparison of diffusion frame to the bond vectors and structure for F177R1 (A) and the immobile component of I204R1 (B). The van der Waals surface, including hydrogen atoms, is shown as a gray mesh around the stick representation of both structures. The two images represent different views (180° rotation) in order to view the diffusion frame in relation to the side chain bonds, nitroxide, and surrounding environment. The van der Waals surface of the surrounding environment, excluding hydrogen atoms, is shown as a translucent light gray surface around stick representations of the contacting residues. The rotational diffusion frame coordinates from the solution EPR spectral fit of F177R1 and the immobile component of I204R1 are superimposed on the stick representation of the spin labels. The rates of rotation about the diffusion axes are higher about the y_R axis, suggesting the spin label is fluctuating mostly about the terminal bond nearest the ring (χ_5) while confined to contacts made with the environment.

and membrane proteins (Figure 2) were solely due to the polarity of solvent (water versus alkyl chains of detergent), the room temperature F177R1 X- and Q-band EPR spectra were simulated using the anisotropic-order χ_4/χ_5 motional model for SEHS of soluble proteins (*10*) and the magnetic parameters determined for the detergent-exposed site. Rates and order were allowed to vary to obtain the best fit while restricting β_D and α_D to 36° and 4° ± 10°, respectively (Figure 11A,B and Table 3). The anisotropic-order χ_4/χ_5 model fits using the magnetic parameters for the hydrophobic environment indicate that the central line differences between soluble and membrane SEHS can be accounted for by the difference in polarity. Also, the broadening observed in the EPR line shape of lipid/detergent-exposed nitroxides compared to soluble proteins is not due to the increased oxygen concentration in the interior of the micelle or lipid bilayer (Figure S6). However, the overall spectral fit at both X- and Q-band indicates the anisotropic-order χ_4/χ_5 model fits are too sharp especially in the high-field manifold (highlighted with the gray box in Figure 11). In the anisotropic-order χ_4/χ_5 model, the sharp features are due to the ordering potential about the z-axis of the diffusion tensor, and lowering the potential and decreasing the rates (to compensate for the lower ordering potential) were not sufficient to fit the broad line shape observed in the experimental spectrum (Figure S7A). In order to explore alternative motional models, the F177R1 EPR spectrum was simulated, allowing the diffusion angles as well as the rates and order to vary in order to obtain the best fit (Figure 11C,D and Table 3). Compared to the anisotropic-order χ_4/χ_5 model fit, the new set of Euler angles and diffusion parameters improve the fit of the entire spectrum significantly, decreasing the reduced χ^2 from 22 to 17.

Theoretical Fits of F177R1. The spectrum of F177R1 is best fit with highly anisotropic rates and an α_D of −57° (Table 3). With axially symmetric magnetic parameters and similar rates ($R_x \approx R_y$), α_D values have no influence on the EPR spectrum; however, in this case neither the rates nor magnetic parameters are axial symmetric and α_D has a significant effect on the EPR line shape (Figure S8). With an α_D of −57°, y_R is almost coincident with the χ_5 bond axis (differing by 8°; Figures 12A and 13C); therefore, motions about y_R average mostly y- and z-magnetic parameters. The z-axis of the diffusion frame, z_R, and the ordering potential are aligned with z_M (the molecular z-axis; see Figure 4). In contrast, the anisotropic-order χ_4/χ_5 model, with a β_D of 41°, tilts z_R and the ordering potential toward the molecular x-axis (x_M), and motion about y_R averages z- and x-elements of the magnetic tensor (Figure S9A).

With the alternative orientation of the diffusion frame (α_D = −57°), the anisotropic rates ($R_y > R_x > R_z$, where R_i is the rotational rate about the i diffusion axis reported as $\log(R_i/s^{-1})$) can be interpreted in terms of the F177R1 crystal structure (Figure 12A). The dominant rate is R_y, which arises from oscillations about χ_5 and results in ring rotation. The correlation time for R_y oscillation (and thereby oscillations about χ_5) is on the order of the overall internal side chain dynamics observed at SEHS in T4L (*10*). Depending on the conformation of the ring, oscillations about χ_4 average the magnetic parameters differently. In the conformation observed in the crystal structure, motion about χ_4 would have mostly an R_x component and very little

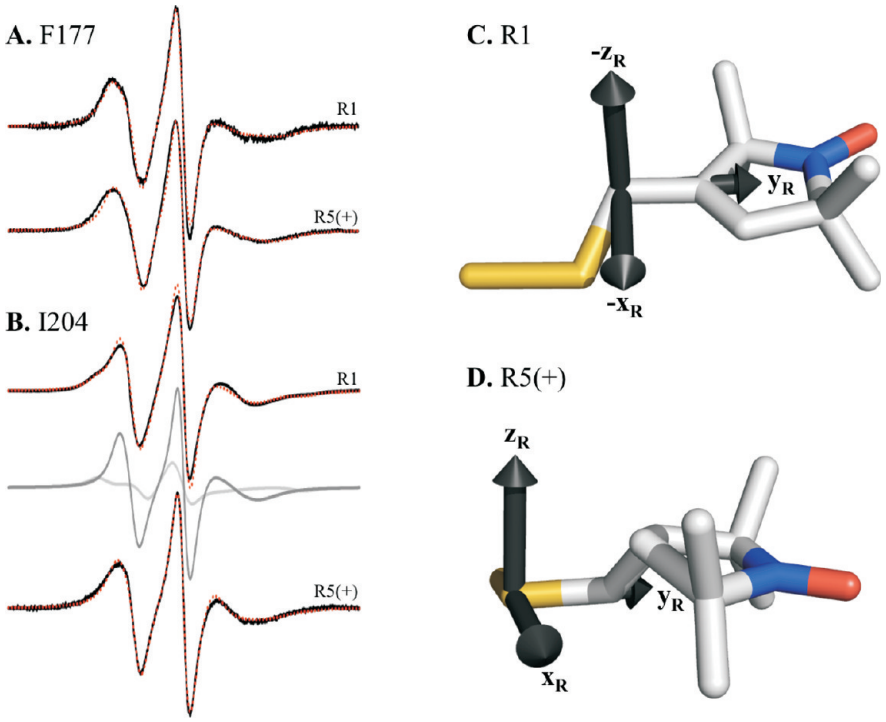

FIGURE 13: Theoretical fits of LeuT EPR spectra. (A, B) The experimental spectra (black) and theoretical fits (dotted red, superimposed) are shown for F177R1/R5(+) and I204R1/R5(+). For I204R1, the EPR spectral fit for each population is shown in gray (α) and light gray (β). (C) The side chain structures of R1 and R5(+) with the orientation of the diffusion frame shown as black arrows. Translational motion is not detected in EPR spectroscopy; therefore, the diffusion frame is arbitrarily positioned on C_ε (R1) and S_δ (R5(+)) for comparison to oscillations about χ_5 and χ_4, respectively.

R_z contribution. However, if the ring, via oscillations about χ_5, were positioned perpendicular to that observed in the crystal structure, then R_z would reflect χ_4 oscillations. Motion about R_z is much slower than R_x, consistent with the observed structure. The spectral fits are insensitive to changes in $R_z < 7$ (16 ns), and only an upper bound on the rate is determined (Figure S10). The theoretical fits are in agreement with the crystal structure: R_y represents oscillations about χ_5, R_x represents oscillations about χ_4 (slower than R_y, but faster than R_z), and R_z is slow and not representative of oscillations about χ_4 and/or χ_5.

An interesting result of spectral fitting is the lack of a large ordering potential considering the interactions the nitroxide has with the protein and the slow rates (R_x and R_z) that reflect these interactions. An order parameter of 0.24 (corresponding to a mean angular displacement of z_R of $\langle\theta\rangle = 45°$) yields the best fit of F177R1, which is smaller than that observed for spin-labeled SEHS on T4L ($S = 0.35-0.40$ ($\langle\theta\rangle = 41-39°$)) (*10*). The EPR spectrum of F177R1 (and R1 on membrane proteins in general) has a very broad high-field manifold, which cannot be simulated using high ordering potentials and high rates (Figure S7B). Although increasing the order parameter increases the breadth of the spectrum, increasing the order parameter also sharpens features of the spectrum (due to resolving the parallel (z_M) and perpendicular (x_M and y_M) magnetic parameters) not observed in the spectra of F177R1 (Figure S7B).

The anisotropic-rate χ_4/χ_5 model derived from theoretical fits to the F177R1 EPR spectrum is consistent with the structure. The interaction between the ring and the surface of the protein results in highly anistropic motion of the nitroxide ring with faster motions (with restricted amplitude of motion) about axes rotating the ring on the surface (R_x and R_y) and slower motions that result in the ring moving off the protein surface (R_z).

Theoretical Fits of I204R1. The EPR spectrum of I204R1 was fit with two spectral components (Figure 13B). The mobile component, α (68% populated), can be fit with the anisotropic-rate χ_4/χ_5 model used to fit the EPR spectrum of F177R1 (Figure 13A, R1, and Table 3); however, R_y and R_z are higher and the ordering potential is lower than for F177R1. The immobile spectral component, β (32% populated), is fit with slower rates, lower amplitude of motion, and a larger α_D compared to both F177R1 and the mobile component of I204R1. The data indicate the crystal structure of I204R1 most closely represents the β spectral population; however, comparing the motional model derived from theoretical fits to the crystal structure, as was done for F177R1, is complicated by the significant degeneracy of the fits as represented by the large range of dynamic parameters for the I204R1 β-component (Table S1). With this caveat notwithstanding, an α_D of ~±90° places the fastest rotating diffusion frame axis, y_R, collinear with the nitroxide bond (Figure 12B), which is involved in a nontraditional hydrogen bond with F208. The large ordering parameter indicates that the oscillation of the motion about y_R (as well as x_R) is highly restricted in amplitude, consistent with the nitroxide ring interaction with the surface of the protein (Figure 12B). Although restricted, the β-population is not entirely rigid. The measured $2A_{zz}$ value of 62 G is lower than the 69 G expected for an immobilized spin label in an aliphatic environment.

EPR Spectra, Theoretical Fits, and Motional Models of F177R5 and I204R5. To investigate the effect nitroxide ring geometry has on the motion of the spin label, the saturated analogue to R1, R5(±), was employed. For R1, χ_4 and χ_5 have relatively low barriers of rotation and can easily exchange between multiple rotamers at room temperature (*37*). The χ_5 axis is parallel to the plane of the nitroxide ring (in between the molecular *x*- and *y*-axes), whereas the χ_4 axis is nearly coaxial

with the molecular *z*-axis (Figures 1 and 13C). Changing the hybridization (sp^2 to sp^3) of the three and four carbon atoms of the ring moves the distal sulfur closer to the plane of the nitroxide ring and, thus, provides greater conformational restriction about χ_5 (Figures 13D and S9).

However, χ_4 remains unrestricted in R5 and is free to contribute to the mobility of the nitroxide ring. In addition to these steric differences, the geometrical relationship between the two terminal bonds nearest the nitroxide ring and the magnetic frame is altered. For R5(+), the χ_5 axis is positioned nearly coaxial with the molecular *z*-axis. In this configuration, motion about χ_5 averages the *x*- and *y*-components of the magnetic tensor and, assuming the lowest energy conformation of χ_5 (~180°; $S_\delta-C_\varepsilon-C_3-C_2$) for R5(+), the χ_4 axis is positioned between the molecular *x*- and *y*-axes. The change in bond geometry between R1 and R5(+) and its effect on the motional model of the spin labels on soluble proteins were previously elucidated (*10*).

Theoretical fits to spectra of R5 on T4L indicated that changing the Euler angles relating the diffusion frame to the magnetic frame while maintaining relatively isotropic rotational rates reproduced the apparent change in mobility. The change in Euler angles moves the director (ordering potential) ~60° toward the plane of the ring and nearly coincident with the N−O bond (Figure S9B). The positioning of the ordering potential parallel to the plane of the nitroxide suggests motion of the spin label is more restricted about χ_5 and less restricted about χ_4 (*10*, *15*). Further supporting the model, small 4-substituents do not significantly reduce the amplitude of R5 motion as they do for R1 (*10*).

Panels A and B of Figure 13 show the EPR spectra for F177R5(+) and I204R5(+), respectively. The spectra of the enantiomers are nearly identical (data not shown). The F177R5-(+) and I204R5(+) spectrum is similar to R1 (the mobile α-component for I204), and the theoretical fits are similar with small increases in rates (Table 3). In contrast to the model used to fit spectra of R1 on T4L, the anisotropic-rate χ_4/χ_5 model of R1 on membrane protein SEHS has anisotropic rates of motion with a moderate to low ordering potential. A change in Euler angles changes not only the relationship between the ordering potential and the magnetic frame but also the anisotropic-rate distribution with respect to the magnetic frame. Therefore, the I204R5(+) and F177R5(+) spectra could not be adequately fit with similar changes in Euler angles. Figure 13C,D shows the structure of R1 and R5(+) with the diffusion frame positioned based on the Euler angles obtained from theoretical fits of F177R1/R5(+). In the case of R1, the diffusion frame *y*-axis is nearly collinear with χ_5 whereas in the case of R5 y_R is nearly collinear with χ_4. This suggests, as in the case with R1 and R5(+) on T4L, the dominant motion of R1 and R5(+) is due to oscillations about χ_4 and χ_5, respectively, consistent with the rotational barriers for each of the spin labels.

Theoretical Fits As a Function of Temperature. To investigate the activation barriers of nitroxide motion, each spectrum of the temperature series was fit allowing rotational rates to vary. Figure 14A,B shows an Arrhenius plot of the average rotational rate ($\langle R\rangle = [R_xR_yR_z]^{1/3}$) determined from the theoretical fits of the F177R1 and I204R1 spectra, respectively, at different temperatures (Table S2). Because the spectra are rather insensitive to changes in R_z (fits can be obtained for $R_z < 7$; Figure S10), R_z was kept nearly constant for all fits. The order parameter was allowed to vary but only within the relative uncertainty reported (range reported in Table S1); most order

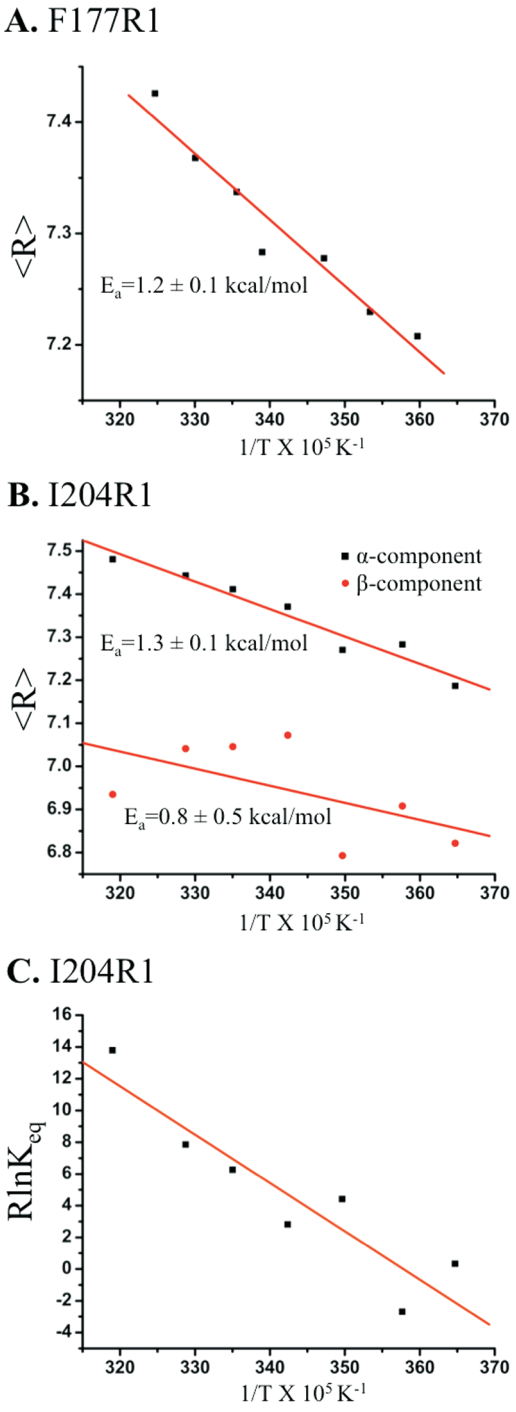

FIGURE 14: Arrhenius plots for F177R1 (A) and I204R1 (B) and van't Hoff plot for K_{eq} (α/β) for I204R1 (C). The linear least-squares fit for F177R1 and the mobile α-component of I204R1 both have an $R^2 = 0.97$. The linear least-squares fit for the immobile β-component of I204R1 has an $R^2 = 0.57$, and the van't Hoff plot has an $R^2 = 0.92$. The van't Hoff plot data are fit with a straight line with the slope corresponding to $\Delta H = 7 \pm 1.4$ kcal mol^{-1} and a *y*-intercept given by $\Delta S = 26 \pm 5$ cal mol^{-1} K^{-1}.

parameter values deviated by less than 10% (Table S2). The $\langle R\rangle$ versus 1/K data for F177R1, as well as the mobile component of I204R1, are fit with a straight line with a slope corresponding to an activation energy of ≈1.2 kcal mol^{-1}. The immobile component data could not be fit well. The spectral fits to the immobile component are more degenerate as can be seen in the ranges of values that produce satisfactory fits (Table S1). Although the ranges of rates and order for acceptable fits of the immobile

component are larger, the relative population does not change significantly for each fit within these ranges; therefore, the temperature dependence of the equilibrium constant can be investigated. Figure 14C shows the van't Hoff plot for K_{eq} (α/β) for I204R1. The data are fit with a straight line with the slope corresponding to $\Delta H \approx 7$ kcal mol^{-1} and a y-intercept given by $\Delta S \approx 30$ cal mol^{-1} K^{-1}.

DISCUSSION

Observed Interactions of R1 on Membrane Protein SEHS. Previous structural studies of R1 on SEHS of T4L have provided the structural basis for a motional model for the internal nitroxide dynamics on soluble proteins (the anisotropic-order χ_4/χ_5 model). In several crystal structures, the nitroxide side chain electron density was observed out to S_δ, but not for the nitroxide ring due to dynamic or static disorder (*11*−*14*). Although many structures of spin labels on T4L have been determined, relatively few conformers of R1 were observed, and most were stabilized by a C_α−H···S_δ interaction. The consequence of this interaction is restricted oscillations about the χ_1 and χ_2 dihedral bonds. The results presented in this study suggest the nitroxide side chain at comparable SEHS on α-helical membrane proteins (facing the hydrophobic detergent rather than aqueous solvent) maintains the C_α−H···S_δ interaction, while, in contrast to soluble proteins, the nitroxide ring interacts with the protein surface. The interpretation of the structures of R1 presented here, which were determined at 100 K, in terms of the solution EPR spectra requires some indirect investigations, such as mutagenesis and temperature dependence of the EPR spectra. Additional experiments, such as room temperature crystal structures and EPR spectra of the protein crystals, which would aid in comparing the low temperature crystal structure to the EPR spectra in solution at room temperature, were not feasible due to the size of the LeuT crystals and degradation of the crystals in the X-ray beam at room temperature. However, spectra of F177R1 and I204R1 do not change in the presence of PEG 550 concentrations up to 14% (Figure S11), and previous investigations of 18 structures of R1 on T4L indicate only one structure had an additional rotamer weakly observed at 298 K that was not observed at 100 K (*11*−*14*).

In both structures of the R1 spin label on LeuT, the entire nitroxide side chain electron density is observed. Both of the observed conformers for R1 at sites F177 and I204 contain a C_α−H···S_δ interaction (Table 2) with the mean distance between S_δ and C_α (3.4 Å), closer than the mean distance observed for spin labels in the same conformation on T4L (3.5 Å) (*11*−*14*). Therefore, this interaction appears to be slightly stronger in the low dielectric of the micelle interior, supporting the postulate that the attractive interaction between the two atoms is a nontraditional hydrogen bond (*11*, *14*).

The calculated fits to the experimental spectra as well as the crystal structures of F177R1 and I204R1 suggest that the spin label has a greater affinity for its protein environment at SEHS on membrane proteins than on similar sites on aqueous proteins. Although the physical driving force for this interaction is not known, there is evidence that membrane proteins have similar energetic contributions to side chain burial as soluble proteins (*39*) and that membrane proteins have more of the available surface area buried than soluble proteins (*40*). In addition, multiple studies investigating the distribution of side chain rotamers between membrane proteins and soluble proteins have shown that relative populations of rotamers are different for membrane proteins and soluble proteins (*41*, *42*) and that the rotamers in membrane proteins bury more surface area (*41*). The role of the solvent (detergent or lipid) in mediating the side chain packing is unknown; however, there is evidence that the lack of water may be a sufficient driving force. Bryant and co-workers observed that the side chains of dry (lyophilized) BSA or BSA in DMSO are densely packed on the protein surface and have limited flexibility compared to hydrated BSA (*43*), suggesting the interaction of water with the protein surface could displace the spin label on T4L and, thus, cause the spin label to be more mobile. The EPR data coupled with crystallography provide a method to probe dynamics and side chain interactions (e.g., buried surface area) and compare the stabilizing forces that drive membrane and soluble protein folding.

Origins of the Two Spectral Components of I204R1. The EPR spectrum of I204R1 has two spectral components similar to many SEHS on membrane proteins (Figure 2). The crystal structure of I204R1 is of a single conformer and appears to correspond to the immobile β-spectral component, but the origin of the mobile α-component is unknown. The mobile component of I204R1 is very similar to F177R1, which has many interactions with the protein surface indicating that the spectra could represent a side chain rotamer in which the side chain interacts with a different region of the protein surface surrounding position I204. The two spectral components could arise from different side chain rotamers, backbone conformations, or both. The R5 derivative and the van't Hoff plot suggest the different spectral components arise from side chain rotamers.

The single component spectrum for I204R5(+) (Figure 13) suggests the environment of the saturated spin label is more similar to the mobile component of the I204R1 spectrum and may be attributed to the change in geometry from R1 to R5 disrupting the immobilizing nontraditional hydrogen bond interaction observed in the crystal structure of I204R1. In addition, the R5 single spectral component implies that the two spectral components of I204R1 arise from R1 conformers and not from protein conformational states.

The van't Hoff plot also provides some insight in understanding the origin of the two spectral components of I204R1. The difference in enthalpy between the two populations is ≈7 kcal mol^{-1}. The observed nontraditional hydrogen bond is approximated to be 2 kcal mol^{-1} (*44*−*47*), and the stability of the conformer in the crystal structure due to the buried surface area (70 Å^2) can be approximated to be 2 kcal mol^{-1} (*39*). Thus, assuming a dominantly enthalpic component for each of these two interactions, the magnitude of the energetic differences between the spectral populations obtained from the van't Hoff plot is close to the value expected for different side chain conformers. However, small changes in the secondary or tertiary structure of LeuT could also contribute to the difference in enthalpy between the populations.

If the two spectral components are side chain rotamers, one possible origin is disulfide isomerization. Molecular dynamic simulations of the spin label on polyalanine helices suggest disulfide isomers of R1 may have significantly different environments that lead to multiple component spectra (*48*). Modeling the disulfide isomers of I204R1 suggests each conformation, $\chi_3 \approx 90°$ and $\chi_3 \approx -90°$, would have significantly different motional constraints. The spin label observed in the crystal structure of I204R1, $\chi_3 \approx -90°$, makes multiple contacts with the protein surface and is likely restricted in mobility. In contrast, modeling of the spin label in the alternate conformation of the disulfide,

$\chi_3 \approx +90°$, suggests the spin label makes fewer contacts with the protein surface and, therefore, would be more mobile. Saturation recovery data of I204R1 indicate the exchange rate between the two spectral components is ~100 kHz or slower (B. Kroncke, M. Bridges, W. L. Hubbell, and L. Columbus, unpublished), which is slower than the ~1.0−70 MHz expected for isomerization of the disulfide (*17*). Although the exchange rate is slower than observed, the isomerization barrier could be modulated by the $C_\alpha-H\cdots S_\delta$ interaction and/or additional interactions between the nitroxide and protein surface, which could destabilize the transition state by the ~2 kcal mol^{-1} needed to slow the exchange rate to ~100 kHz.

Nitroxide Side Chain Rotamers on Transmembrane α-Helices. The only R1 rotamers observed on SEHS of soluble proteins are {**m**,**m**}, {**t**,**p**}, and {**t**,**m**} (*11*). In this study, the two R1 rotamers on SEHS of a membrane protein were {**m**,**m**}, one of the two conformers ({**m**,**m**} and {**t**,**p**}) on an α-helix that allow a $C_\alpha-H\cdots S_\delta$ interaction. In both cases reported here, the side chain could adopt the {**t**,**p**} rotamer without steric clash; nonetheless, it is not observed. Unlike most of the SEHS structures of R1 on T4L, the entire side chain is resolved in the F177R1 and I204R1 structures though the $\chi_3-\chi_5$ dihedral angle values differ between the two (Table 2). The allowed dihedral angles of the disulfide, χ_3, are −90° and +90°, and both are observed for I204R1 and F177R1, respectively. In a relaxed side chain, χ_4 and χ_5 are expected to be in a *trans* conformer; however, both F177R1 and I204R1 deviate significantly from these values due to interactions between the nitroxide ring and residues within the same α-helix (I204R1) or a neighboring helix (F177R1).

Anisotropic-Rate χ_4/χ_5 Model. The spectra of R1 on SEHS of membrane proteins are distinct from analogous sites on soluble proteins. The fit to F177R1 shows that the broad line features of membrane protein EPR spectra can be partially reproduced by adjusting the magnetic components of the **g**- and **A**-tensor to reflect the lower polarity of the environment (Figure 11); however, the anisotropic-order χ_4/χ_5 model does not reproduce the broad features of the high-field line of F177R1 (Figure 11). The features of the high-field and low-field line are best reproduced by using an anisotropic diffusion tensor in which the fastest motion is about the diffusion frame *y*-axis and the amplitude restriction is about the molecular/diffusion frame *z*-axis. To test the general applicability of the anisotropic-rate χ_4/χ_5 model, spectra of EmrE and MsbA at solvent-exposed sites in DDM were simulated (Figure S12) (*49*, *50*). The calculated spectra capture the salient features of the experimental spectra and suggest the model has more general applicability beyond the sites investigated in this study.

For both fits of F177R1 and I204R1 (mobile α-component), the rotational rates of the diffusion frame are highly anisotropic. The position of the diffusion frame places the fastest rotating axis, y_R, nearly coaxial with the terminal bond of the spin label, χ_5. The fast rates about y_R suggest that the most significant source of motion of the spin label comes from rotations about χ_5. Previously, 4-position derivatives of the nitroxide ring were used to investigate the contributions of χ_5 by sterically hindering rotations about the terminal bond nearest the nitroxide ring (*15*). On T4L SEHS the methyl derivative, R2, was sufficient to significantly hinder the nitroxide motion (*15*). At F177 and I204, a 4-Br derivative, R7, significantly reduces the mobility of the spin label (B. Kroncke and L. Columbus, unpublished), indicating that oscillations about χ_5 are the dominant contributions to the nitroxide motions (although the possibility of a gained interaction between the protein surface and the 4-substituent cannot be excluded). In the anisotropic-order χ_4/χ_5 model for aqueous SEHS and the anisotropic-rate χ_4/χ_5 model for the aliphatic SEHS, oscillations about χ_5 significantly contribute to the motional averaging of the nitroxide ring. However, in the hydrophobic environment, electron density for the ring is resolved and the overall correlation time of R1 is longer than analogous sites on T4L, ~6 ns versus ~2 ns (*10*), respectively. The slower motion indicates an additional steric restriction of R1 on SEHS on membrane proteins compared to T4L sites in which ring electron density is not observed and the overall correlation time of R1 is lower. In combination with the crystal structures of R1, these data suggest the motion of the spin label is greatly influenced by the protein surface. Despite these interactions with the protein surface, the nitroxide motions giving rise to the spectral averaging (oscillations about χ_4 and χ_5) have low activation energies.

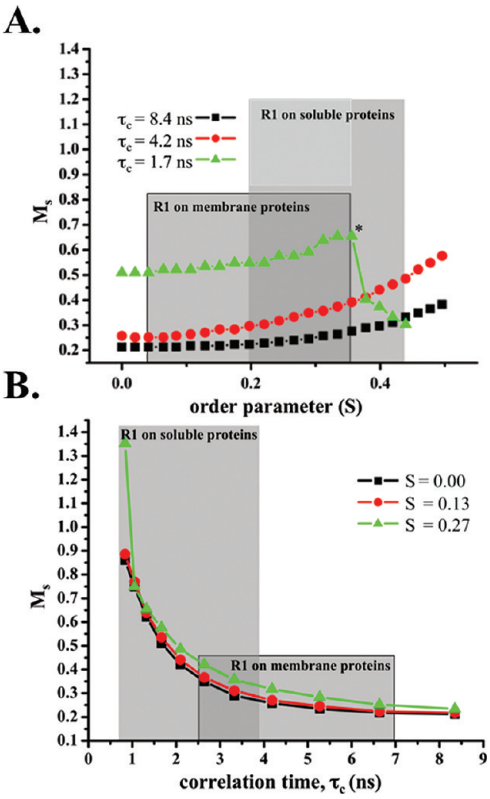

FIGURE 15: Dependence of M_s on S_{20} and τ_c determined from spectra simulated using the anisotropic-rate χ_4/χ_5 model. M_s is defined as the scaled experimentally measured inverse center line width: $M_s = (\delta_{exp}^{-1} - \delta_i^{-1})/(\delta_m^{-1} - \delta_i^{-1})$. (A) Dependence of M_s on the order parameter for the indicated correlation times. (B) Dependence of M_s on correlation time for the anisotropic-rate χ_4/χ_5 model. δ_i and δ_m were defined according to scale determined by Columbus et al. (*3*) as 8.4 and 2.1 G, respectively. The ranges for M_s observed for R1 on membrane proteins and on soluble proteins are highlighted in gray. For short τ_c and S_{20}, greater than ~0.35, **g**-tensor anisotropy is resolved, resulting in much lower M_s values (indicated by the asterisk). The form of M_s (S_{20}, τ_c) for the model presented here is similar to that predicted by the anisotropic-order χ_4/χ_5 model (*2*), with a stronger dependence on τ_c.

The activation energy barrier of the nitroxide side chain, E_a, in the limited temperature range between 274 and 311 K, is equal to the sum of the activation barrier of viscous flow, E_η, and the intrinsic activation barrier of rotation, E_i ($E_a = E_\eta + E_i$). The measured activation barrier for both F177R1 and the α-component of I204R1 is ≈1.2 kcal mol^{-1}, which is lower than the ~6 kcal mol^{-1}

reported for D72R1 on T4L in 30% sucrose. The difference in E_a between the LeuT and T4L SEHS is likely due to the difference in solvent viscosity between 30% sucrose and the aliphatic environment of the detergent micelle. For D72R1 T4L, the activation barrier was determined to be due solely to the activation barrier of viscous flow of the 30% sucrose solution (*10*). Although the activation energy for viscous flow in the interior of the OG micelle is not known, the activation energy for viscous flow was determined to be 2.2 and 3.6 kcal mol^{-1} for toluene and *n*-hexadecane, respectively (*51*), and 3.8 kcal mol^{-1} in hexadecyltrimethylammonium chloride (CTACl) micelles (*52*), similar to values measured here.

Measuring Membrane Protein Dynamics. A simple method for extracting protein dynamics from EPR spectra is to plot the EPR scaled mobility, M_s, versus residue. ($M_s = (\delta_{exp}^{-1} - \delta_i^{-1})/(\delta_m^{-1} - \delta_i^{-1})$ where δ_{exp}, δ_m, and δ_i are the experimentally measured, most mobile, and most immobile central line widths observed for all R1-labeled proteins, respectively (*3*).) A plot of M_s versus residue correlates protein motion, including backbone fluctuations and steric environment, and protein sequence (*3*, *53*). Several SDSL studies have correlated α-helical backbone motions with structure and function for soluble proteins (*1*−*3*, *54*). For membrane proteins, the range of M_s values observed is lower in scale and amplitude, and the physical origin of the observed dampening is not known (*3*). The different magnetic parameters and potentially different motional models of membrane SEHS modulate the sensitivity of M_s to backbone fluctuations (Figure 15). The results of this study indicate the motional model is different; however, the dependence of M_s on the amplitude and rate of the nitroxide motion (Figure 15) is similar to that of the anisotropic-order χ_4/χ_5 model (*2*). The lower M_s values for membrane proteins appear to originate from the restricted rate of nitroxide motion due to weak interactions between the ring and the protein surface. The dampening of the overall differences between M_s values on membrane SEHS results from the lower average correlation times of the spin label, τ_c. In the regime of τ_c predicted from the anisotropic-rate χ_4/χ_5 model presented here, $\tau_c \approx 2.5-7.0$ ns, M_s is less sensitive to changes in rate and amplitude of motion (Figure 15).

The spectra of F177R1 and the mobile component of I204R1 are fit with the anisotropic-rate χ_4/χ_5 model; therefore, differences in the rates and ordering potential may reflect backbone dynamic modes regardless of the interactions the ring has with the protein surface. The overall rotational rate and amplitude of motion for I204R1 are slightly larger than for F177R1. In order to suggest possible differences in backbone mobility, the crystallographic *B*-factors in the wild-type structure were compared. The *B*-factors for F177C_α and I204C_α are 20 and 27 Å^2, respectively, and the average *B*-factor for two helical turns within the helices (residues 171−177 and 198−204) is 18 and 26 Å^2 for helices 4 and 5, respectively. The increase in the disorder of helix 5 is likely due to a proline kink introduced at residue P200. Several studies have shown an increase in backbone flexibility due to proline kinks in transmembrane helices (*55*, *56*), and the EPR spectrum of I204R1 may reflect this flexibility.

CONCLUSION

In summary, the results presented in this investigation provide a motional model for R1 on SEHS of membrane proteins and suggest that SDSL, coupled with theoretical spectral fitting, can be used to quantify membrane protein dynamics. EPR spectra of SEHS on membrane proteins in the low dielectric of the detergent micelle are distinct from their soluble homologues and cannot be reproduced by simple changes to the aqueous protein model of spin label motion such as changing magnetic parameters, rate, and/or order. The data presented support an anisotropic-rate χ_4/χ_5 model of internal motion in which R1 is influenced mostly by oscillations about the terminal bond nearest the nitroxide ring while maintaining weak contacts with the protein surface. The motion of this terminal bond is modulated by the quantity and type of contacts made with the protein surface and yields the variety of spectra observed for R1 on membrane proteins.

Although the neighboring residues and solvent are largely different between soluble proteins and membrane proteins, the $C_\alpha-H\cdots S_\delta$ interaction appears to be as strong, if not stronger, in the lower dielectric than in the aqueous environment. The attractive interaction between these atoms has been shown to restrict the motion of the first two dihedral angles of R1, causing EPR spectra to be sensitive to backbone motion of the protein. However, in membrane proteins, the sensitivity to backbone motion is damped and complicated by interactions between the nitroxide ring and the protein surface. Additional studies need to be conducted that investigate the diversity of interactions, rotamers, and motional models of R1 on membrane proteins in order to fully realize the quantitative applications of SDSL and EPR to functional backbone motions.

One useful application of nitroxides is distance determination in biomolecules, such as nitroxide−nitroxide distances with pulsed EPR or nitroxide−nuclei distances with NMR. The resolution and interpretation of these distances are dependent on knowledge of the spin label position (*22*, *23*). In both aqueous and membrane environments, oscillations about the spin label's $\chi_1-\chi_3$ dihedral angles is restricted and partially restricting the conformational space of the spin label. The data presented suggest the local environment of the spin label determines the three terminal dihedral angles nearest the ring of R1 and that R1 on the surface of membrane proteins has a smaller spatial distribution due to interactions with the protein surface. These structures provide the beginnings of an R1 rotamer library at SEHS of membrane proteins, which will increase the precision of spin label positioning on membrane proteins and, thus, provide better interpretation of nitroxide-derived distances and distance distributions.

ACKNOWLEDGMENT

We thank Dr. Michael C. Wiener for X-ray crystallography support, Izabela Bielnicka for technical assistance, and Alison Dewald and Dan Freed for critical reading of the manuscript.

SUPPORTING INFORMATION AVAILABLE

Two tables containing theoretical fit ranges and parameters and further details of background EPR signal and structural influences of EPR spectra. This material is available free of charge via the Internet at http://pubs.acs.org.

REFERENCES

1. McHaourab, H. S., Lietzow, M. A., Hideg, K., and Hubbell, W. L. (1996) Motion of spin-labeled side chains in T4 lysozyme. Correlation with protein structure and dynamics. *Biochemistry 35*, 7692–7704.
2. Columbus, L., and Hubbell, W. L. (2004) Mapping backbone dynamics in solution with site-directed spin labeling: GCN4-58 bZip free and bound to DNA. *Biochemistry 43*, 7273–7287.
3. Columbus, L., and Hubbell, W. L. (2002) A new spin on protein dynamics. *Trends Biochem. Sci. 27*, 288–295.

4. Fanucci, G. E., and Cafiso, D. S. (2006) Recent advances and applications of site-directed spin labeling. *Curr. Opin. Struct. Biol. 16*, 644–653.
5. Hubbell, W. L., Cafiso, D. S., and Altenbach, C. (2000) Identifying conformational changes with site-directed spin labeling. *Nat. Struct. Mol. Biol. 7*, 735–739.
6. Lietzow, M. A., and Hubbell, W. L. (2004) Motion of spin label side chains in cellular retinol-binding protein: correlation with structure and nearest-neighbor interactions in an antiparallel beta-sheet. *Biochemistry 43*, 3137–3151.
7. Ladner, C. L., Chen, M., Smith, D. P., Platt, G. W., Radford, S. E., and Langen, R. (2010) Stacked sets of parallel, in-register beta-strands of beta2-microglobulin in amyloid fibrils revealed by site-directed spin labeling and chemical labeling. *J. Biol. Chem. 285*, 17137–17147.
8. Tong, J., Borbat, P. P., Freed, J. H., and Shin, Y. K. (2009) A scissors mechanism for stimulation of SNARE-mediated lipid mixing by cholesterol. *Proc. Natl. Acad. Sci. U.S.A. 106*, 5141–5146.
9. Amadi, S. T., Koteiche, H. A., Mishra, S., and McHaourab, H. S. (2010) Structure, dynamics, and substrate-induced conformational changes of the multidrug transporter EmrE in liposomes. *J. Biol. Chem. 285*, 26710–26718.
10. Columbus, L., Kalai, T., Jeko, J., Hideg, K., and Hubbell, W. L. (2001) Molecular motion of spin labeled side chains in alpha-helices: analysis by variation of side chain structure. *Biochemistry 40*, 3828–3846.
11. Fleissner, M. R., Cascio, D., and Hubbell, W. L. (2009) Structural origin of weakly ordered nitroxide motion in spin-labeled proteins. *Protein Sci. 18*, 893–908.
12. Guo, Z., Cascio, D., Hideg, K., and Hubbell, W. L. (2008) Structural determinants of nitroxide motion in spin-labeled proteins: solvent-exposed sites in helix B of T4 lysozyme. *Protein Sci. 17*, 228–239.
13. Guo, Z., Cascio, D., Hideg, K., Kalai, T., and Hubbell, W. L. (2007) Structural determinants of nitroxide motion in spin-labeled proteins: tertiary contact and solvent-inaccessible sites in helix G of T4 lysozyme. *Protein Sci. 16*, 1069–1086.
14. Langen, R., Oh, K. J., Cascio, D., and Hubbell, W. L. (2000) Crystal structures of spin labeled T4 lysozyme mutants: implications for the interpretation of EPR spectra in terms of structure. *Biochemistry 39*, 8396–8405.
15. McHaourab, H. S., Kalai, T., Hideg, K., and Hubbell, W. L. (1999) Motion of spin-labeled side chains in T4 lysozyme: effect of side chain structure. *Biochemistry 38*, 2947–2955.
16. Fleissner, M. R., Brustad, E. M., Kalai, T., Altenbach, C., Cascio, D., Peters, F. B., Hideg, K., Schultz, P. G., and Hubbell, W. L. (2009) Site-directed spin labeling of a genetically encoded unnatural amino acid. *Proc. Natl. Acad. Sci. U.S.A. 106*, 21637–21642.
17. Fraser, R. R., Boussard, G., Saunders, J. K., Lambert, J. B., and Mixan, C. E. (1971) Barriers to rotation About sulfur-sulfur bond in acyclic disulfides. *J. Am. Chem. Soc. 93*, 3822.
18. Budil, D. E., Lee, S., Saxena, S., and Freed, J. H. (1996) Nonlinear-least-squares analysis of slow motion EPR spectra in one and two dimensions using a modified Levenberg-Marquardt algorithm. *J. Magn. Reson. 120*, 155–189.
19. Yamashita, A., Singh, S. K., Kawate, T., Jin, Y., and Gouaux, E. (2005) Crystal structure of a bacterial homologue of Na^+/Cl^--dependent neurotransmitter transporters. *Nature 437*, 215–223.
20. Altenbach, C., Flitsch, S. L., Khorana, H. G., and Hubbell, W. L. (1989) Structural studies on transmembrane proteins. 2. Spin labeling of bacteriorhodopsin mutants at unique cysteines. *Biochemistry 28*, 7806–7812.
21. Lovell, S. C., Word, J. M., Richardson, J. S., and Richardson, D. C. (2000) The penultimate rotamer library. *Proteins 40*, 389–408.
22. Sale, K., Song, L. K., Liu, Y. S., Perozo, E., and Fajer, P. (2005) Explicit treatment of spin labels in modeling of distance constraints from dipolar EPR and DEER. *J. Am. Chem. Soc. 127*, 9334–9335.
23. Liang, B., Bushweller, J. H., and Tamm, L. K. (2006) Site-directed parallel spin-labeling and paramagnetic relaxation enhancement in structure determination of membrane proteins by solution NMR spectroscopy. *J. Am. Chem. Soc. 128*, 4389–4397.
24. Klock, H. E., and Lesley, S. A. (2009) The polymerase incomplete primer extension (PIPE) method applied to high-throughput cloning and site-directed mutagenesis. *Methods Mol. Biol. 498*, 91–103.
25. Warkentin, M., and Thorne, R. E. (2009) Slow cooling and temperature-controlled protein crystallography. *J. Struct., Funct., Genomics 8*, 141–144.
26. Otwinowski, Z., and Minor, V. (1997) Processing of X-ray diffraction data collected in oscillation mode. *Methods Enzymol. 276*, 307–326.
27. Collaborative Computational Project Number 4 (1994) The CCP4 suite: programs for protein crystallography. *Acta Crystallogr., Sect. D: Biol. Crystallogr. 50*, 760–763.
28. Emsley, P., and Cowtan, K. (2004) Coot: model-building tools for molecular graphics. *Acta Crystallogr., Sect D: Biol. Crystallogr. 60*, 2126–2132.
29. Davis, I. W., Leaver-Fay, A., Chen, V. B., Block, J. N., Kapral, G. J., Wang, X., Murray, L. W., Arendall, W. B., III, Snoeyink, J., Richardson, J. S., and Richardson, D. C. (2007) MolProbity: all-atom contacts and structure validation for proteins and nucleic acids. *Nucleic Acids Res. 35*, W375–383.
30. DeLano, W. L. (2002) The PyMOL Molecular Graphics System, DeLano Scientific, San Carlos, CA.
31. Smith, J. L., Hendrickson, W. A., Honzatko, R. B., and Sheriff, S. (1986) Structural heterogeneity in protein crystals. *Biochemistry 25*, 5018–5027.
32. Baker, E. N., and Hubbard, R. E. (1984) Hydrogen bonding in globular proteins. *Prog. Biophys. Mol. Biol. 44*, 97–179.
33. Gross, A., Columbus, L., Hideg, K., Altenbach, C., and Hubbell, W. L. (1999) Structure of the KcsA potassium channel from Streptomyces lividans: a site-directed spin labeling study of the second transmembrane segment. *Biochemistry 38*, 10324–10335.
34. Altenbach, C., Yang, K., Farrens, D. L., Farahbakhsh, Z. T., Khorana, H. G., and Hubbell, W. L. (1996) Structural features and light-dependent changes in the cytoplasmic interhelical E-F loop region of rhodopsin: a site-directed spin-labeling study. *Biochemistry 35*, 12470–12478.
35. Altenbach, C., Marti, T., Khorana, H. G., and Hubbell, W. L. (1990) Transmembrane protein structure: spin labeling of bacteriorhodopsin mutants. *Science 248*, 1088–1092.
36. Altenbach, C., Greenhalgh, D. A., Khorana, H. G., and Hubbell, W. L. (1994) A collision gradient method to determine the immersion depth of nitroxides in lipid bilayers: application to spin-labeled mutants of bacteriorhodopsin. *Proc. Natl. Acad. Sci. U.S.A. 91*, 1667–1671.
37. Tombolato, F., Ferrarini, A., and Freed, J. H. (2006) Dynamics of the nitroxide side chain in spin-labeled proteins. *J. Phys. Chem. B 110*, 26248–26259.
38. Owenius, R. (2001) Influence of solvent polarity and hydrogen bonding on the EPR parameters of a nitroxide spin label studied by 9-GHz and 95-GHz EPR spectroscopy and DFT calculations. *J. Phys. Chem. A 105*, 10967–10977.
39. Faham, S., Yang, D., Bare, E., Yohannan, S., Whitelegge, J. P., and Bowie, J. U. (2004) Side-chain contributions to membrane protein structure and stability. *J. Mol. Biol. 335*, 297–305.
40. Oberai, A., Joh, N. H., Pettit, F. K., and Bowie, J. U. (2009) Structural imperatives impose diverse evolutionary constraints on helical membrane proteins. *Proc. Natl. Acad. Sci. U.S.A. 106*, 17747–17750.
41. Chamberlain, A. K., and Bowie, J. U. (2004) Analysis of side-chain rotamers in transmembrane proteins. *Biophys. J. 87*, 3460–3469.
42. Hong, H., Joh, N. H., Bowie, J. U., and Tamm, L. K. (2009) Methods for measuring the thermodynamic stability of membrane proteins. *Methods Enzymol.: Biothermodyn. 455* (Part A), 213–236.
43. Goddard, Y. A., Korb, J. P., and Bryant, R. G. (2006) Structural and dynamical examination of the low-temperature glass transition in serum albumin. *Biophys. J. 91*, 3841–3847.
44. Barth, P., Schonbrun, J., and Baker, D. (2007) Toward high-resolution prediction and design of transmembrane helical protein structures. *Proc. Natl. Acad. Sci. U.S.A. 104*, 15682–15687.
45. Gu, Y. L., Kar, T., and Scheiner, S. (1999) Fundamental properties of the CH···O interaction: Is it a true hydrogen bond? *J. Am. Chem. Soc. 121*, 9411–9422.
46. Scheiner, S., Kar, T., and Gu, Y. L. (2001) Strength of the (CH)-H-alpha···O hydrogen bond of amino acid residues. *J. Biol. Chem. 276*, 9832–9837.
47. Vargas, R., Garza, J., Dixon, D. A., and Hay, B. P. (2000) How strong is the C-alpha-H···O=C hydrogen bond? *J. Am. Chem. Soc. 122*, 4750–4755.
48. Sezer, D., Freed, J. H., and Roux, B. (2008) Parametrization, molecular dynamics simulation, and calculation of electron spin resonance spectra of a nitroxide spin label on a polyalanine alpha-helix. *J. Phys. Chem. B 112*, 5755–5767.
49. Amadi, S. T., Koteiche, H. A., Mishra, S., and McHaourab, H. S. (2010) Structure, dynamics, and substrate-induced conformational changes of the multidrug transporter EmrE in liposomes. *J. Biol. Chem. 285*, 26710–26718.
50. Zou, P., and McHaourab, H. S. (2009) Alternating access of the putative substrate-binding chamber in the ABC transporter MsbA. *J. Mol. Biol. 393*, 574–585.
51. Glowinkowski, S., Gisser, D. J., and Ediger, M. D. (1990) C-13 nuclear-magnetic-resonance measurements of local segmental dynamics of polyisoprene in dilute-solution—nonlinear viscosity dependence. *Macromolecules 23*, 3520–3530.

52. Laguitton-Pasquier, H., Pansu, R., Chauvet, J. P., Pernot, P., Collet, A., and Faure, J. (1997) 10,10′-Bis(2-ethylhexyl)-9,9′-bianthryl (BOA) molecule: the first free aromatic probe for the core of micelles. *Langmuir 13*, 1907–1917.
53. Hubbell, W. L., McHaourab, H. S., Altenbach, C., and Lietzow, M. A. (1996) Watching proteins move using site-directed spin labeling. *Structure 4*, 779–783.
54. Van Eps, N., Oldham, W. M., Hamm, H. E., and Hubbell, W. L. (2006) Structural and dynamical changes in an alpha-subunit of a heterotrimeric G protein along the activation pathway. *Proc. Natl. Acad. Sci. U.S.A. 103*, 16194–16199.
55. Cordes, F. S., Bright, J. N., and Sansom, M. S. (2002) Proline-induced distortions of transmembrane helices. *J. Mol. Biol. 323*, 951–960.
56. Thomas, R., Vostrikov, V. V., Greathouse, D. V., and Koeppe, R. E., 2nd (2009) Influence of proline upon the folding and geometry of the WALP19 transmembrane peptide. *Biochemistry 48*, 11883–11891.
57. Langen, R., Isas, J. M., Hubbell, W. L., and Haigler, H. T. (1998) A transmembrane form of annexin XII detected by site-directed spin labeling. *Proc. Natl. Acad. Sci. U.S.A. 95*, 14060–14065.
58. Salwinski, L., and Hubbell, W. L. (1999) Structure in the channel forming domain of colicin E1 bound to membranes: the 402−424 sequence. *Protein Sci. 8*, 562–572.
59. Altenbach, C., Greenhalgh, D. A., Khorana, H. G., and Hubbell, W. L. (1994) A collision gradient method to determine the immersion depth of nitroxides in lipid bilayers: application to spin-labeled mutants of bacteriorhodopsin. *Proc. Natl. Acad. Sci. U.S.A. 91*, 1667–1671.
60. Holm, L., and Park, J. (2000) DaliLite workbench for protein structure comparison. *Bioinformatics 16*, 566–567.